NEW TECHNOLOGIES FOR CANCER

IMMUNOTHERAPY AND DISEASE PROFILING

by
Chih-Ping Mao

A dissertation submitted to The Johns Hopkins University in conformity with the
requirements for the degree of Doctor of Philosophy

Baltimore, Maryland
October 2017

Abstract

Mutant tumor antigens have recently emerged as major targets of endogenous tumor-specific T cells. Vaccination against these neoantigens therefore provides the opportunity to augment antitumor lymphocyte responses. In this context, we developed a technology to prime and expand desired populations of antigen-specific T cells based on programmed self-assembly of cognate peptide-MHC (pMHC). We capitalized on the unique properties of the protein annexin V (ANXA5) to couple the early onset of TCR signaling to stabilization of pMHC-TCR interactions, repeated pMHC encounter, and extensive TCR crosslinking. This system amplified lymphocyte activation by over 1,000-fold, bypassed the need for costimulation, and overcame tolerance to a model self-antigen *in vivo*. These studies lay the foundation for immune modulation via a positive feedback-driven self-assembly platform. Furthermore, we created a single-molecule imaging approach for quantitative and structural analysis of circulating mutant tumor proteins, which may ultimately be applied to identify tumor neoantigens. We demonstrated in preclinical models that mutant tumor proteins are released from tumor cells into the blood early in tumor progression. We then utilized this technology to profile circulating mutant p53 in ovarian cancer patients. Single-molecule structural analysis revealed that, in a subset of patients, circulating mutant p53 aggregates into complexes. Moreover, patients lacking circulating mutant p53 displayed abundant anti-p53 autoantibodies, suggesting that host immune responses clear mutant tumor antigens from the blood. Finally, we propose that structural analysis of circulating mutant tumor proteins by single-molecule imaging may be employed to discover and screen tumor neoantigens for vaccination.

Thesis advisors

T.-C. Wu, M.D., Ph.D.

Professor of Pathology, Oncology, Obstetrics and

Gynecology, and Molecular Microbiology and Immunology

Director, Division of Gynecologic Pathology

Chien-Fu Hung, Ph.D.

Associate Professor of Pathology and Oncology

Acknowledgements

I would also like to thank those in the MD/PhD Program, including Dr. Robert Siliciano, Dr. Andrea Cox, Sharon Welling, Bernardine Harper, and Martha Buntin, as well as the Immunology Graduate Program, including Dr. Mark Soloski, Dr. Joel Pomerantz, Angela James, and Lori Fountain, for all of their help and advice.

Finally, I dedicate this work to my parents, whose love and care are the reason I am here today.

Table of Contents

List of Figures

Chapter 2.

I. Chapter 1. An integrated paradigm of cancer immunotherapy and disease profiling.

Introduction: a brief history of cancer immunotherapy. The original idea of invigorating the host immune system to combat cancer dates back to the work of Coley in the early 1900s[1]. Shortly afterwards, this concept was superseded in the clinical arena by prominent advances in chemotherapy and radiotherapy, though key insights into the relationship between cancer and the immune system continued to be uncovered in the laboratory. In the 1950s, Ehrlich, Burnet, and Thomas posited that the adaptive immune system constantly scans the body for and eliminates malignant cells[2]; as a corollary to this, cancer arises from defective immune surveillance. In the early 2000s, nearly a century since Coley, the theory of cancer immune editing was unveiled, portraying a dual role of the immune system in both promoting cancer in some instances and curbing its growth in others[3].

The discovery of the intricate interactions between cancer and the immune system—catalyzed by an explosion in the understanding of immune pathways and major advances in molecular biology—has fueled tremendous enthusiasm for leveraging the immune system to control cancer.

Indeed, in recent years immunotherapy has raced to the forefront of novel interventions for cancer[4]. The discovery, for instance, that costimulatory signals are essential for full lymphocyte activation, and that CTLA-4[5] on T cells competes with CD28 for B7 costimulatory signals on antigen-presenting cells[6], thereby shutting down these T

cells, led to the use of antagonist CTLA-4 antibodies to augment antitumor immune responses, first in mice[7] and then in melanoma patients[8, 9]. Similarly, antibodies that block a separate immune checkpoint pathway, the programmed death-1 (PD-1) receptor and its ligand (PD-L1)[10, 11], have produced cancer regression in a substantial number of patients across a broad spectrum of cancer types, including melanoma, non-small cell lung cancer, colorectal cancer, and renal cell carcinoma[12]. Outside of checkpoint inhibitors, adoptive transfer of tumor-reactive T cells has also shown modest clinical success thus far[13]. For instance, Rosenberg and colleagues reported 50% partial or complete responses in melanoma patients treated by adoptive therapy[14]. In addition, in a study of adoptive therapy with chimeric antigen receptor-bearing T cells modified to recognize CD19 in acute lymphoblastic leukemia, complete remission was observed in 90% of patients[15].

Barriers to clinical success. Altogether, these clinical data underscore the potential of the immune system to control cancer. By harnessing the exquisitely specific, self-propagating nature and long-term memory of T cells, immunotherapy offers the hope of lasting disease control[16]. However, T cells rarely clear tumor cells completely from the body. In fact, most patients undergoing immunotherapy still fail to mount any noticeable antitumor immune responses or eventually experience disease relapse[16].

Accumulating evidence indicates that tumor cells employ myriad mechanisms to evade host immune defenses, including: downregulation of MHC class I, β2 microglobulin, or antigen-processing machinery[16, 17]; production of inhibitory enzymes (e.g., IDO, arginase) or cytokines (e.g., IL-10, TGF-β)[18]; recruitment of suppressive subsets of cells (e.g., regulatory T cells, immature myeloid cells)[19-24]; gain of survival factors[16]; and

elaboration of checkpoint molecules (e.g., PD-L1, CTLA-4), which turn off tumor-specific T cells[25].

In light of these many immune escape mechanisms and the diversity of immune responses seen in patients, it is important to explore the key determinants of durable antitumor responses. Vigorous efforts are currently underway to dissect the mechanisms that underlie durable responses—or lack thereof—to immunotherapy.

The tumor microenvironment as a permissive site for launching tumor-specific immune responses. One central idea is that—although tumor cells have been sculpted through the process of immune editing[26]—through the expression of unique mutant or ectopic antigens, the tumor has a natural tendency to provoke antitumor immune responses, and the number of pre-existing functional tumor-specific lymphocyte precursors may govern both disease outcome and responses to therapy. In a landmark study, Galon *et al.* established that the abundance of T cells within tumor tissue strongly predicts prognosis, even more so than conventional TNM staging[27]. Likewise, in cervical cancer patients, a high density of CD8$^+$ T cells in the tumor correlated with absence of metastasis and prolonged survival[28, 29]. These results indicate that the immune system is on its own capable of mounting cytotoxic responses against tumor cells, and the magnitude of these responses dictates to a large extent disease outcome. In our own work, we found that antigen exposure within the tumor—as occurs following chemotherapy—stimulates tumor-specific CD8$^+$ T cells via the type I IFN pathway[30]. Consistent with this, clinical responses to PD-1 blockade depended on the presence of pre-existing CD8$^+$ T cells in the tumor vicinity[31]. Collectively, these data argue that the availability of endogenous tumor-specific lymphocyte precursors is a critical determinant of antitumor immune responses. It is therefore essential develop

3

strategies to firstly identify and secondly amplify dormant populations of these lymphocyte precursors.

The emerging landscape of tumor neoantigens. The activation and expansion of rare tumor-specific lymphocyte populations first requires uncovering the antigens against which they react. The clinical progress that has been achieved by checkpoint blockade therapy, together with technical advances in whole-exome sequencing, has provided the opportunity to investigate the cognate antigens of tumor-specific T cells. For example, Gubin *et al.* found through bioinformatics techniques in preclinical sarcoma models that these T cells predominately recognize mutant antigens[32]. Consistent with this, in cancer patients, clinical benefit is associated with an extensive load of mutant tumor proteins[33, 34], specific mutant neoepitopes[35, 36], and DNA mismatch repair defects[37]. Together, these results imply that host T cells efficiently spot mutant antigens displayed by tumor cells. Capitalizing on this idea, in a proof-of-principle study, Kreiter *et al.* designed peptides against mutant antigens and demonstrated tumor rejection in preclinical models[38].

Approaches to generate T cells against mutant tumor are therefore likely to elicit durable antitumor immune responses. Though neoantigens are in principle unique to tumor cells and hence less susceptible to central tolerance than tumor-associated antigens[39], neoantigens may nonetheless exhibit weak affinity for cognate TCR, as is almost universally the case of self-antigens. To address this challenge, we introduce a novel vaccination technology based on programmed self-assembly of peptide-MHC (pMHC). This technology opens the opportunity to amplify endogenous lymphocyte responses to mutant tumor antigens.

Early detection and disease profiling as critical elements of effective immunotherapy. Although immunotherapy has transformed the landscape of cancer management, this type of therapy is likely most effective for early-stage disease, while the tumor has not yet grown beyond the capacity of T cells to control it. As the tumor expands, immune-suppressive networks thrive and nutrients are depleted, rendering the tumor microenvironment inhospitable for infiltrating T cells. Indeed, it is well-established that early cancer detection and intervention improves clinical outcome. For instance, cancer morbidity and mortality occurs commonly due to late disease diagnosis, and epidemiologic data illustrate that the most lethal cancer types, such as ovarian or pancreatic cancer, are also those which are hardest to identify. Thus, vaccination against mutant tumor antigens holds the greatest probability of success early in the course of disease, highlighting the urgent need for advances in cancer detection. Furthermore, accurate, rapid profiling of mutant tumor antigens is equally important to identify suitable candidates for vaccination.

Conventional assays for tumor proteins, such as those that screen for CA-125 (in ovarian cancer) or PSA (in prostate cancer), lack the sensitivity and specificity demanded for reliable early cancer detection and cannot be applied for profiling mutant tumor antigens[40-44]. The concept of 'liquid biopsies', revolving around the detection of circulating tumor DNA via next-generation sequencing, has recently shown promise[45]. However, while these approaches have improved dramatically from a technical standpoint in recent years[45], they still miss the disease in approximately 50% of patients with stage I or II cancer[46]. Furthermore, circulating tumor DNA does not provide information about gene expression within the tumor, or about the structural or functional features of altered oncoproteins and tumor suppressor proteins.

To address the need for early cancer detection and profiling methods, we invented a single-molecule imaging technology to identify circulating mutant tumor proteins, as well as autoantibodies to these proteins. By imaging these mutant proteins at single-molecule resolution, we can deduce their structural and functional properties, a feat that cannot be attained by other methods. We foresee that this imaging platform may be utilized to: (1) identify the presence of cancer and (2) characterize mutant antigens amenable to immunotherapy.

New technologies for cancer immunotherapy and disease profiling. In **Chapter 2,** we build on the compelling idea that tumor neoantigens can be targeted via rational vaccination strategies to amplify antigen-specific lymphocyte responses. We present a programmable vaccination approach to engineer signaling events at the level of pMHC-TCR interactions to—in a concerted manner—stabilize pMHC-TCR binding, facilitate serial pMHC encounter, and induce TCR crosslinking. We demonstrate that this technology markedly augments lymphocyte activation and overcomes immune tolerance to low-affinity antigens, which may be useful in raising responses against mutant tumor proteins.

In **Chapter 3,** we present a single-molecule imaging approach to identify mutant tumor proteins early—at a stage in which the disease has a high chance of being successfully managed by immunotherapy—and to characterize its structural and functional features. We believe that this approach offers the potential to catch cancer early and to pinpoint the characteristics of the tumor most amenable to therapy.

Finally, in **Chapter 4,** we lay out our vision for how these technologies can be integrated to build a comprehensive next-generation immunotherapy platform. We propose

that single-molecule imaging can serve as a powerful tool to simultaneously identify and

screen mutant tumor neoantigens, selecting those which are most likely to engender robust,

durable clinical responses.

References

1. Coley, W.B. The Treatment of Inoperable Sarcoma by Bacterial Toxins (the Mixed Toxins of the Streptococcus erysipelas and the Bacillus prodigiosus). *Proc R Soc Med* **3**, 1-48 (1910).

2. Burnet, F.M. Immunological surveillance in neoplasia. *Transplant Rev* **7**, 3-25 (1971).

3. Dunn, G.P., Bruce, A.T., Ikeda, H., Old, L.J. & Schreiber, R.D. Cancer immunoediting: from immunosurveillance to tumor escape. *Nat Immunol* **3**, 991-998 (2002).

4. Miller, J.F. & Sadelain, M. The journey from discoveries in fundamental immunology to cancer immunotherapy. *Cancer Cell* **27**, 439-449 (2015).

5. Brunet, J.F. et al. A new member of the immunoglobulin superfamily--CTLA-4. *Nature* **328**, 267-270 (1987).

6. Krummel, M.F. & Allison, J.P. CD28 and CTLA-4 have opposing effects on the response of T cells to stimulation. *J Exp Med* **182**, 459-465 (1995).

7. Leach, D.R., Krummel, M.F. & Allison, J.P. Enhancement of antitumor immunity by CTLA-4 blockade. *Science* **271**, 1734-1736 (1996).

8. Hodi, F.S. et al. Improved survival with ipilimumab in patients with metastatic melanoma. *N Engl J Med* **363**, 711-723 (2010).

9. Robert, C. et al. Ipilimumab plus dacarbazine for previously untreated metastatic melanoma. *N Engl J Med* **364**, 2517-2526 (2011).

10. Dong, H., Zhu, G., Tamada, K. & Chen, L. B7-H1, a third member of the B7 family, co-stimulates T-cell proliferation and interleukin-10 secretion. *Nat Med* **5**, 1365-1369 (1999).

11. Freeman, G.J. et al. Engagement of the PD-1 immunoinhibitory receptor by a novel B7 family member leads to negative regulation of lymphocyte activation. *J Exp Med* **192**, 1027-1034 (2000).

12. Zou, W., Wolchok, J.D. & Chen, L. PD-L1 (B7-H1) and PD-1 pathway blockade for cancer therapy: Mechanisms, response biomarkers, and combinations. *Sci Transl Med* **8**, 328rv324 (2016).

13. Fesnak, A.D., June, C.H. & Levine, B.L. Engineered T cells: the promise and challenges of cancer immunotherapy. *Nat Rev Cancer* **16**, 566-581 (2016).

14. Rosenberg, S.A. et al. Durable complete responses in heavily pretreated patients with metastatic melanoma using T-cell transfer immunotherapy. *Clin Cancer Res* **17**, 4550-4557 (2011).

15. Maude, S.L. et al. Chimeric antigen receptor T cells for sustained remissions in leukemia. *N Engl J Med* **371**, 1507-1517 (2014).

16. Sharma, P., Hu-Lieskovan, S., Wargo, J.A. & Ribas, A. Primary, Adaptive, and Acquired Resistance to Cancer Immunotherapy. *Cell* **168**, 707-723 (2017).

17. Marincola, F.M., Jaffee, E.M., Hicklin, D.J. & Ferrone, S. Escape of human solid tumors from T-cell recognition: molecular mechanisms and functional significance. *Adv Immunol* **74**, 181-273 (2000).

18. Motz, G.T. & Coukos, G. Deciphering and reversing tumor immune suppression. *Immunity* **39**, 61-73 (2013).

19.	Arina, A. & Bronte, V. Myeloid-derived suppressor cell impact on endogenous and adoptively transferred T cells. *Curr Opin Immunol* **33**, 120-125 (2015).

20.	Biswas, S.K. & Mantovani, A. Macrophage plasticity and interaction with lymphocyte subsets: cancer as a paradigm. *Nat Immunol* **11**, 889-896 (2010).

21.	Marigo, I. et al. Tumor-induced tolerance and immune suppression depend on the C/EBPbeta transcription factor. *Immunity* **32**, 790-802 (2010).

22.	Bonertz, A. et al. Antigen-specific Tregs control T cell responses against a limited repertoire of tumor antigens in patients with colorectal carcinoma. *J Clin Invest* **119**, 3311-3321 (2009).

23.	Mosser, D.M. & Edwards, J.P. Exploring the full spectrum of macrophage activation. *Nat Rev Immunol* **8**, 958-969 (2008).

24.	van der Burg, S.H. et al. Association of cervical cancer with the presence of CD4+ regulatory T cells specific for human papillomavirus antigens. *Proc Natl Acad Sci U S A* **104**, 12087-12092 (2007).

25.	Pardoll, D.M. The blockade of immune checkpoints in cancer immunotherapy. *Nat Rev Cancer* **12**, 252-264 (2012).

26.	Schreiber, R.D., Old, L.J. & Smyth, M.J. Cancer immunoediting: integrating immunity's roles in cancer suppression and promotion. *Science* **331**, 1565-1570 (2011).

27.	Galon, J. et al. Type, density, and location of immune cells within human colorectal tumors predict clinical outcome. *Science* **313**, 1960-1964 (2006).

28.   de Vos van Steenwijk, P.J. et al. An unexpectedly large polyclonal repertoire of HPV-specific T cells is poised for action in patients with cervical cancer. *Cancer Res* **70**, 2707-2717 (2010).

29.   Piersma, S.J. et al. High number of intraepithelial CD8+ tumor-infiltrating lymphocytes is associated with the absence of lymph node metastases in patients with large early-stage cervical cancer. *Cancer Res* **67**, 354-361 (2007).

30.   Kang, T.H. et al. Chemotherapy acts as an adjuvant to convert the tumor microenvironment into a highly permissive state for vaccination-induced antitumor immunity. *Cancer Res* **73**, 2493-2504 (2013).

31.   Tumeh, P.C. et al. PD-1 blockade induces responses by inhibiting adaptive immune resistance. *Nature* **515**, 568-571 (2014).

32.   Gubin, M.M. et al. Checkpoint blockade cancer immunotherapy targets tumour-specific mutant antigens. *Nature* **515**, 577-581 (2014).

33.   Rizvi, N.A. et al. Cancer immunology. Mutational landscape determines sensitivity to PD-1 blockade in non-small cell lung cancer. *Science* **348**, 124-128 (2015).

34.   Snyder, A. et al. Genetic basis for clinical response to CTLA-4 blockade in melanoma. *N Engl J Med* **371**, 2189-2199 (2014).

35.   Linnemann, C. et al. High-throughput epitope discovery reveals frequent recognition of neo-antigens by CD4+ T cells in human melanoma. *Nat Med* **21**, 81-85 (2015).

36.   van Rooij, N. et al. Tumor exome analysis reveals neoantigen-specific T-cell
       reactivity in an ipilimumab-responsive melanoma. *J Clin Oncol* **31**, e439-442
       (2013).

37.   Le, D.T. et al. PD-1 Blockade in Tumors with Mismatch-Repair Deficiency. *N
       Engl J Med* **372**, 2509-2520 (2015).

38.   Kreiter, S. et al. Mutant MHC class II epitopes drive therapeutic immune
       responses to cancer. *Nature* **520**, 692-696 (2015).

39.   Yarchoan, M., Johnson, B.A., 3rd, Lutz, E.R., Laheru, D.A. & Jaffee, E.M.
       Targeting neoantigens to augment antitumour immunity. *Nat Rev Cancer* **17**, 209-
       222 (2017).

40.   Galli, C., Basso, D. & Plebani, M. CA 19-9: handle with care. *Clin Chem Lab
       Med* **51**, 1369-1383 (2013).

41.   Sikaris, K.A. CA125--a test with a change of heart. *Heart Lung Circ* **20**, 634-640
       (2011).

42.   Mazzucchelli, R., Colanzi, P., Pomante, R., Muzzonigro, G. & Montironi, R.
       Prostate tissue and serum markers. *Adv Clin Path* **4**, 111-120 (2000).

43.   Ruibal Morell, A. CEA serum levels in non-neoplastic disease. *Int J Biol Markers*
       7, 160-166 (1992).

44.   Wanebo, H.J. et al. Preoperative carcinoembryonic antigen level as a prognostic
       indicator in colorectal cancer. *N Engl J Med* **299**, 448-451 (1978).

45.   Wan, J.C. et al. Liquid biopsies come of age: towards implementation of
       circulating tumour DNA. *Nat Rev Cancer* **17**, 223-238 (2017).

46. Phallen, J. et al. Direct detection of early-stage cancers using circulating tumor DNA. *Sci Transl Med* **9** (2017).

II.   Chapter 2. Programmed self-assembly of peptide-MHC for antigen-specific immune modulation

A technology to prime any desired population of T cells in the body—particularly those that possess low avidity against target antigen—would pave the way to the design of new types of vaccination for intractable infectious diseases or cancer. Here we report such a technology based on positive feedback-driven, programmed self-assembly of peptide-MHC (pMHC) directly on the membrane of cognate T cells. Our design capitalizes on the unique features of the protein annexin V (ANXA5), which—in a concerted and synergistic manner—couples the early onset of TCR signaling by cognate pMHC with a surge in pMHC-TCR affinity, with repeated pMHC encounter, and with widespread TCR crosslinking. In our system, ANXA5 is linked to pMHC and firmly engages the plasma membrane of cognate T cells upon (and only upon) the early onset of TCR signaling. ANXA5 in turn exerts a mechanical force that stabilizes interactions at the TCR-pMHC interface and facilitates repeated, serial pMHC encounter. Furthermore, ANXA5 quickly arranges into uniform 2D matrices, thereby prompting TCR crosslinking. Fusion of ANXA5 to pMHC augments lymphocyte activation by several orders of magnitude (>1,000-fold), bypasses the need for costimulation, and breaks tolerance against a model self-antigen *in vivo*. Our study opens the door to the application of synthetic, feedback-driven self-assembly platforms in immune modulation.

Due to their unique capacity to recognize a nearly infinite array of antigen variants with exquisite sensitivity, T cells have the potential to eradicate many types of diseases, from those caused by external pathogens to those caused by transformation from within (i.e. cancer). In many instances, however, activation of a desired population of T cells by vaccination remains an elusive challenge. For example, in the case of cancer, although it has been shown that T cells can play a key role in the control of tumor progression[1-5], tumor-specific T cells almost universally suffer from a poor capacity to recognize tumor antigen due to intricate mechanisms of central and peripheral immune tolerance[6, 7]. We thought that activation and expansion of any desired population of T cells could be achieved by precisely engineering the cascade of molecular events at the level of interactions between the TCR and cognate peptide-MHC (pMHC), as this is a major control point for the ultimate fate of T cells. In particular, it has been established that the avidity of T cells for their target antigen is dictated by the affinity[8-10], frequency[11-13], and valency[14, 15] of interactions between TCR and cognate pMHC. In fact, in order for T cells to undergo full activation and expansion in response to antigen encounter, they must exhibit a high TCR affinity for cognate pMHC ('kinetic proofreading' model)[8-10], sample the antigen persistently ('serial triggering' model)[11-13], or acquire high TCR occupancy by pMHC ('valency' model)[14, 15].

We reasoned that the simultaneous fulfillment of all these criteria would pave the way to the activation of low avidity T cells. We further deduced that high TCR affinity could be realized by imposing a mechanical force at the molecular level to stabilize interactions with cognate pMHC (analogous to a super-antigen), that serial TCR triggering would occur if cognate pMHC was held in the vicinity of TCR, and that high TCR

occupancy could be attained by extensive TCR crosslinking. In conjunction, these events would synergistically amplify signaling through the TCR, resulting in the robust activation of even low avidity T cells.

Here we report a technology to accomplish this based on programmed self-assembly of pMHC on the membrane of cognate T cells. We constructed a system in which a 'dynamic anchor' couples the early onset of TCR signaling by cognate pMHC with a surge in pMHC-TCR affinity, with repeated pMHC encounter, and with widespread TCR crosslinking. To achieve this, we programmed the dynamic anchor to sense and react to certain microenvironmental cues. In particular, the dynamic anchor: (1) exclusively recognizes antigen-specific T cells in a positive feedback-driven process catalyzed by the onset of TCR signaling, (2) attaches tightly to the membrane of these T cells, and (3) undergoes rapid self-assembly upon binding to the membrane. Our design incorporates the protein annexin V (ANXA5) as a dynamic anchor and exploits several unique features of this protein and its phospholipid receptor, phosphatidylserine (PS). First, ANXA5 has a high affinity for PS (K_D~10^{-10} M) under physiologic calcium concentrations. Second, we have mapped the kinetics of PS exposure on T cells and found that PS is externalized rapidly and reversibly in cognate T cells upon TCR signaling by pMHC. And third, ANXA5 is equipped with the remarkable capacity to organize into uniform 2D matrices on the lipid bilayer[16].

We demonstrated that programmed pMHC self-assembly on cognate T cells via the ANXA5 anchor augments antigen-specific lymphocyte activation by over 1,000-fold, bypasses the need for costimulation, and reverses tolerance to self-antigen. We investigated the mechanisms underlying these effects and discovered that ANXA5 fusion overrides low-

affinity pMHC-TCR interactions. Both pMHC tethering and self-assembly by ANXA5 were found to be critical for immune modulation. Furthermore, downstream of initial pMHC encounter, this system instigated TCR crosslinking and internalization. Our results introduce the concept of programmed pMHC self-assembly as a vaccination approach for amplifying lymphocyte responses against low-affinity antigen, such as tumor antigen.

Results

Design and validation of the chimeric ANXA5-pMHC system. We constructed a system in which a 'dynamic anchor' couples the early onset of TCR signaling by cognate pMHC with a surge in pMHC-TCR affinity, with repeated pMHC encounter, and with widespread TCR crosslinking (**Figure II-1a, b**). To achieve this, we programmed the dynamic anchor to sense and react to certain microenvironmental cues. In particular, the dynamic anchor (1) exclusively recognizes antigen-specific T cells in a positive feedback-driven process catalyzed by the onset of TCR signaling, (2) attaches tightly to the membrane of these T cells, and (3) undergoes rapid self-assembly upon binding to the membrane. Our design incorporates the protein ANXA5 as a dynamic anchor and exploits several unique features of this protein and its phospholipid receptor, phosphatidylserine (PS). First, ANXA5 has a high affinity for PS ($K_D \sim 10^{-10}$ M) under physiologic calcium concentrations. Second, we have mapped the kinetics of PS exposure on T cells and found that PS externalizes rapidly and reversibly in cognate T cells upon TCR signaling by pMHC (**Figure II-2a**), with peak PS exposure at ~12 hr followed by full translocation to the inner membrane by 72 hr (**Figure II-2b**). PS exposure also occurred on naïve T cells *ex vivo* in response to CD3 crosslinking (**Figure II-2c**), as close to 80% of stimulated T

cells converted to surface PS$^+$ after 12 hr (**Figure II-2d**). And third, ANXA5 is equipped with the remarkable capacity to organize into uniform 2D matrices on the lipid bilayer[16].

As proof-of-concept, we synthesized a recombinant soluble single-chain pMHC (hereafter referred to as Kb(Ova)) composed of the model H-2K^b-restricted ovalbumin (Ova) epitope (SIINFEKL) linked to β2M and H-2K^b heavy chain carrying deletions in the transmembrane domain and cytoplasmic tail. We then linked the α3 domain of H-2K^b heavy chain in Kb(Ova) to ANXA5 to create chimeric Kb(Ova)/ANXA5 (**Figure II-1b**). To verify pMHC display by the chimeric protein, we incorporated a polyhistidine (His) tag at the C-terminus and synthesized liposomes embedded with nitrilotriacetic acid-nickel (NTA-Ni). We coated Kb(Ova)/ANXA5 or its counterpart control, Kb(Ova), onto NTA-Ni liposomes and probed with antibodies against H-2K^b/SIINFEKL. We determined by flow cytometry that Kb(Ova) and Kb(Ova)/ANXA5 displays similar amounts of H-2K^b/SIINFEKL at >10-fold above background levels (**Supplementary Figure II-1a, b**). Thus, we conclude that fusion to ANXA5 maintains pMHC in an intact state, and effects of the chimeric protein are independent of native pMHC conformation. Next, we confirmed that pMHC/ANXA5 associates with PS phospholipid bilayers. To do so, we synthesized PS$^+$ liposomes to mimic the lymphocyte plasma membrane, pulsed the liposomes with Kb(Ova)/ANXA5 or Kb(Ova) for 30 min, and probed with H-2K^b/SIINFEKL antibodies. PS$^+$ liposomes pulsed with pMHC/ANXA5 displayed 40 times more pMHC than those pulsed with pMHC only (**Supplementary Figure II-2a, b**), indicating that ANXA5 mediates pMHC binding to PS lipid bilayers. Both Kb(Ova)/ANXA5 and Kb(Ova) failed to attach to PS$^-$ liposomes (data not shown). Therefore, we conclude that chimeric pMHC/ANXA5 interacts with and presents antigen on a PS surface.

pMHC fusion to ANXA5 augments cognate lymphocyte activation. Since PS exposure is a feature of apoptosis, we first assessed the survival of T cells in the presence of pMHC/ANXA5 to exclude the potential influence of apoptosis on the behavior of this chimeric protein. T cells treated with Kb(Ova)/ANXA5, ANXA5, Kb(Ova), or no protein demonstrated almost identical viability (~90%) (**Supplementary Figure II-3a, b**), verifying that Kb(Ova)/ANXA5 does not induce lymphocyte apoptosis. To test the function of the pMHC/ANXA5 system, we incubated resting Ova-specific CD8$^+$ T cells (OT-I) with Kb(Ova) or Kb(Ova)/ANXA5 (2.5 μg/ml) and performed flow cytometry after 12 hr to detect IFN-γ expression as an index of activation. At this dose, Kb(Ova)/ANXA5 produced >80% IFN-γ$^+$ T cells, while Kb(Ova) produced <2% IFN-γ$^+$ T cells (**Figure II-3a, b**). Protein titration experiments demonstrated that pMHC/ANXA5 was >1,000× more potent than monomeric pMHC in lymphocyte activation, as defined by the minimal dose of antigen required to detect IFN-γ$^+$ cells (**Figure II-3c**). Notably, Kb(Ova)/ANXA5—but not Kb(Ova)—also induced robust activation of naïve Ova-specific T cells freshly isolated from OT-I transgenic mice without any costimulation (**Figure II-3d**). Cognate lymphocyte activation upon Kb(Ova)/ANXA5 exposure was accompanied by proliferation (**Figure II-3e**). Since it has been shown that activation of T cells by dimeric pMHC is superior to activation by monomeric pMHC[17], we compared activation of T cells by pMHC/ANXA5 versus dimeric pMHC/Fc. Kb(Ova)/ANXA5 was >100× more potent than Kb(Ova)/Fc (**Supplementary Figure II-4a-c**). Moreover, Kb(Ova)/ANXA5 did not elicit IFN-γ expression in non-cognate T cells even at high dose (>10 μg/ml) (data not shown), confirming that activation of T cells by pMHC/ANXA5 is antigen-specific.

19

We inferred that ANXA5-driven programmed pMHC self-assembly may trigger antigen-specific lymphocyte responses *in vivo*. To test this, we first administered either Kb(Ova)/ANXA5 or Kb(Ova) into OT-I TCR transgenic mice. After one day, we measured CD69 expression on CD8$^+$ T cells as a marker of early activation. ~40% of CD8$^+$ T cells in Kb(Ova)/ANXA5-administered mice displayed surface CD69, compared to <2% in Kb(Ova)-administered mice (**Figure II-4a**), suggesting that Kb(Ova)/ANXA5 rapidly induces *in vivo* lymphocyte activation even in the absence of costimulation. In C57BL/6 mice with a diverse lymphocyte TCR repertoire, Kb(Ova)/ANXA5 amplified Ova-specific CD8$^+$ T cells (**Figure II-4b**), indicating that pMHC fusion to ANXA5 expands rare cognate lymphocyte precursors. Consistently, Kb(Ova)/ANXA5 injection led to proliferation of naïve Ova-specific T cells *in vivo,* at ~100-fold lower dose than Kb(Ova) (**Figure II-4c**, **Supplementary Figure II-5**).

By stabilizing low-affinity pMHC-TCR interactions, we reasoned that ANXA5 fusion might overcome immune tolerance to self-antigen. To test this, we employed transgenic mice (232-4) that exhibit ectopic expression of Ova in the intestine[18]. In this model, Ova serves as a self-antigen; therefore, endogenous CD8$^+$ T cells in 232-4 transgenic mice possess tolerance to Ova, and Ova-specific CD8$^+$ T cells cannot be elicited in these mice by conventional methods. Intriguingly, we found that an Ova-specific immune response emerged in 232-4 transgenic mice administered with Kb(Ova)/ANXA5 but not with Kb(Ova) (**Figure II-4d**), suggesting that this technology is able to break immune tolerance to self-antigen.

ANXA5 fusion overcomes low-affinity pMHC-TCR interactions. We wondered whether loss of tolerance to self-antigen might be due to the capacity of the dynamic anchor

to override low-affinity pMHC-TCR interactions. We observed that naïve OT-I cells treated with monomeric Kb(Ova) protein exposed surface PS (**Figure II-5a**), implying that weak pMHC-TCR interactions are sufficient to trigger PS membrane translocation, which propagates pMHC/ANXA5 self-assembly. To directly test the effect of low affinity pMHC-TCR binding on lymphocyte activation, we synthesized a panel of Kb(Ova)/ANXA5 variants with altered peptide ligands (APLs) carrying critical single amino acid substitutions in the Ova epitope that markedly diminish the affinity for TCR (but not for H-2K^b)[19]. We found that when linked to ANXA5, these APLs could induce robust activation of OT-I cells, far superior to the Kb(Ova) control carrying the wildtype SIINFEKL epitope (**Figure II-5b**). Furthermore, the increase in amount of peptide needed to compensate for affinity-dampening mutations in the Ova antigen greatly exceeded the corresponding amount of Kb(Ova) needed (**Figure II-5c**). These results suggest that fusion to ANXA5 overcomes low-affinity pMHC-TCR interactions, bolstering activation of cognate T cells by several orders of magnitude and bypassing the need for costimulation.

Molecular mechanisms underlying lymphocyte activation by pMHC/ANXA5. We reasoned that fusion of ANXA5 to pMHC would tether the pMHC to T cells upon TCR signaling in a positive feedback-driven process (**Figure II-1a**). Thus, chimeric pMHC/ANXA5 would exhibit both a high affinity and frequency of binding to cognate T cells. Consistent with this paradigm, the combined presence of pMHC and ANXA5 lacking a covalent linkage failed to stimulate cognate T cells (**Supplementary Figure II-6**). Moreover, excess soluble ANXA5 could not prevent lymphocyte activation by Kb(Ova)/ANXA5 (**Supplementary Figure II-7**), potentially due to high affinity

attachment of pMHC/ANXA5 to PS externalized upon local TCR membrane signaling, which was not outcompeted by ANXA5.

We employed genetic, biochemical, and functional assays to dissect the mechanisms by which pMHC/ANXA5 operates. As ANXA5 binding to PS requires calcium, we measured lymphocyte activation by pMHC/ANXA5 under different calcium concentrations. Depleting calcium to 33% of physiologic levels impaired OT-I activation by >10-fold, demonstrating strict calcium dependence of pMHC/ANXA5 (**Figure II-6a**). To prove that this calcium dependence traces to disrupted ANXA5 membrane tethering, we synthesized two mutant versions of Kb(Ova)/ANXA5 carrying amino acid substitutions in the calcium-binding domain of ANXA5 (D144N, E228Q or D144N, E228Q, D303N) which abolish interactions between ANXA5 and PS[20]. We confirmed that these mutant proteins could display intact SIINFEKL peptide in the context of H-2K[b] but failed to associate with PS (data not shown). Activation of OT-I cells by mutant Kb(Ova)/ANXA5 proteins was severely impaired compared to wildtype Kb(Ova)/ANXA5 (**Figure II-6b**). Next, we examined the role of self-assembly in the immune-modulating function of ANXA5. To do so, we synthesized a mutant Kb(Ova)/ANXA5 carrying five different amino acid substitutions (R16E, R23E, K27E, K56E, K191E) which prevent self-assembly of ANXA5[21]. We found likewise that loss of self-assembly ability abrogated the capacity of this mutant Kb(Ova)/ANXA5 to stimulate OT-I cells (**Figure II-6c**). Thus, we conclude that—in addition to membrane tethering—instigation of TCR crosslinking by the dynamic anchor is crucial for its ability to evoke lymphocyte activation.

To directly investigate the role of the dynamic anchor in fastening pMHC to the membrane and triggering TCR signaling, we pre-mixed versions of Kb(Ova) or

Kb(Ova)/ANXA5 carrying a His tag with PE-labeled α-His mAb. We then incubated the proteins with OT-I cells at 37°C for 5 hr, and measured pMHC binding and TCR (Vα2) expression by flow cytometry. We found that 98% of OT-I cells incubated with Kb(Ova)/ANXA5:α-His/PE complex became pMHC$^+$ (i.e. displayed PE fluorescence); by contrast, <1% of OT-I cells incubated with Kb(Ova):α-His/PE or with α-His/PE only displayed PE fluorescence (**Figure II-7a**). Moreover, we noticed that—compared to the α-His/PE control—TCR Vα2 expression was downregulated by 90% of OT-I cells incubated with Kb(Ova)/ANXA5:α-His/PE but not by any of those cells incubated with Kb(Ova):α-His/PE (**Figure II-7a**). The TCR is downregulated in T cells as a consequence of TCR engagement by cognate pMHC[22]. Based on these data, we conclude that pMHC/ANXA5 acts on T cells to facilitate repeated, serial encounter with cognate TCR.

To visualize the dynamic anchor-mediated tethering and self-assembly of pMHC on cognate T cells, we incubated Kb(Ova)/ANXA5:α-His/PE or Kb(Ova):α-His/PE with OT-I cells seeded at ultra-low density to prevent any cells from contacting each other and presenting pMHC *in trans*. We then examined individual T cells by epifluorescence single-molecule microscopy to detect (1) total fluorescence as an index of pMHC binding and (2) fluorescence aggregation as an index of pMHC self-assembly. We found that while OT-I cells incubated with α-His/PE or Kb(Ova):α-His/PE displayed extremely low fluorescence, cells incubated with Kb(Ova)/ANXA5:α-His/PE displayed strong fluorescence which tightly clustered at distinct foci (**Figure II-7b**). These data demonstrate the engagement and self-assembly of dynamic anchor-linked pMHC on cognate T cells *in cis*, after which point TCR signaling and crosslinking will proceed.

Discussion

The programmed self-assembly of pMHC we have described represents a powerful approach for the activation of antigen-specific T cells, in particular those that have low affinity for cognate antigen. This approach would be useful for galvanizing a robust immune response against any low avidity tumor or virus antigen. In the field of cancer immunotherapy, ANXA5 fusion to soluble pMHC overcomes two major obstacles faced by vaccination: immune tolerance to tumor self-antigen and the need for functional antigen-presenting cells (APCs) and co-stimulation[23, 24]. With respect to immune self-tolerance, we demonstrated that chimeric pMHC/ANXA5 could stabilize pMHC binding, facilitate repeated TCR encounters, and thereby override low-affinity pMHC-TCR interactions. This strategy is therefore suitable for priming and propagating low avidity endogenous lymphocyte precursors within the tumor. Furthermore, the tumor milieu elaborates a variety of immune-suppressive networks that either deplete or impair the function of APCs, such as dendritic cells[25]. Since conventional vaccination methods rely on a robust pool of APCs to display antigen to cognate T cells[26], these methods are largely unreliable in the tumor microenvironment. By contrast, soluble, chimeric pMHC/ANXA5 proteins directly target and prime antigen-specific T cells independent of APCs. Indeed, we discovered that infusion of these proteins alone could mediate activation of cognate naïve T cells both *in vitro* and within 24 hr post-delivery *in vivo.* Because the dynamic anchor bypasses the need for APCs, this approach is in principle less susceptible to immune suppressive mechanisms in the tumor microenvironment compared conventional vaccination methods.

It is generally believed that full lymphocyte activation requires not only peptide antigen display on MHC proteins but also co-stimulation from proteins such as CD80 and CD86 on APCs, which signal through CD28 on cognate T cells[24]. In this context, it is intriguing that ANXA5 fusion to pMHC circumvents the need for co-stimulation. Although the precise mechanisms for this are unclear, we propose that exponential amplification of total TCR signal strength by ANXA5 pushes T cells past the activation barrier even in the absence of co-stimulation. Consistent with this idea, it has previously been demonstrated that once TCR signal strength reaches a critical threshold, lymphocyte activation occurs regardless of co-stimulation[27].

The proof-of-concept experiments conducted here establish the application of positive feedback driven, self-assembly networks to trigger antigen-specific immune responses. The identification of appropriate tumor antigen candidates will be an important next step in clinical translation. Recent studies employing whole genome sequencing and tumor epitope profiling have revealed that antitumor lymphocyte responses are biased against mutant tumor proteins[13, 28-32]. In this light, we envision that ANXA5 may be linked to mutant antigen peptides on MHC proteins to prime and expand these endogenous tumor-specific T cells. As epitope screening and profiling technologies advance, the ability to quickly raise immune responses against promising antigen candidates becomes critical. We believe the dynamic anchor concept introduced here provides a powerful tool for accomplishing this. Although in our we linked the antigen to a single-chain MHC/ANXA5 molecule via genetic engineering, we foresee that a generic 'empty' MHC/ANXA5 scaffold designed to the MHC haplotype of individual patients could be constructed that may be readily conjugated with any desired epitope of interest via chemical crosslinking.

This could lead to a versatile platform for antigen-specific immune modulation that could be rapidly tailored for different patients.

Moreover, though our approach acts through mechanisms distinct from immune checkpoint blockade, we believe these two types of therapy will be synergistic when administered in combination. In particular, chimeric pMHC/ANXA5 proteins are devised to generate and expand desired populations of antigen-specific T cells, while checkpoint blockade potentiates the function of these T cells by dampening immune suppressive pathways[33]. The synergistic combination of checkpoint blockade with dynamic anchor-based vaccination holds the potential to improve the clinical management of cancer.

An additional important point to address in clinical translation involves the spectrum of target cells that might be recognized by pMHC/ANXA5, as well as the potential regions in the body to which these proteins would traffic. It is well-established, for instance, that apoptotic cells expose surface PS; consequently, a proportion of administered pMHC/ANXA5 would be anticipated to accumulate in injured, infected, or dead tissue. In cancer patients, a substantial amount of pMHC/ANXA5 would likely build up directly in the tumor, as subsets of tumor cells as well as tumor-associated endothelial cells externalize PS[34-36]. In our experiments, we have observed that following systemic injection into tumor-bearing mice, labeled ANXA5 proteins preferentially home to the tumor. In cancer immunotherapy, we believe that the selective delivery of pMHC/ANXA5 represents an advantage of this system, as studies have reported that the presence of tumor-infiltrating T cells is especially important for control of tumor growth[1, 37]. By binding to surface PS on these T cells, pMHC/ANXA5 provides a route to invigorate these local antitumor immune responses.

26

Finally, this approach can be tailored to precisely control the function of antigen-specific T cells in a variety of other ways because the dynamic anchor-pMHC can be readily linked to additional 'cargo' modules. For example, cytokines could be delivered through this technology to amplify the expansion phase of a desired immune response. On the other hand, tolerance-promoting cues could be delivered to repress an autoimmune response. These targeted modalities are in principle far superior—both in terms of safety and efficacy—to conventional methods based on systemic injection of cytokines or other pharmacologic agents because, in this case, the cargo is directed preferentially to an antigen-specific compartment. Furthermore, the general concept of programmed molecular self-assembly could be applied to control other arms of the immune system. For instance, it has been shown that live B cells also expose surface PS in the vicinity of the BCR upon receiving an activation signal[38, 39]. Thus, the dynamic anchor technology could be deployed to raise a strong antibody response against intractable pathogens. We foresee that positive feedback-driven programmed molecular self-assembly will open the doors to the design of new, creative ways to both study and manipulate biological systems.

Methods

Mice. 6- to 8-week old female C57BL/6, OT-I TCR transgenic, and 232-4 transgenic mice were obtained from the National Cancer Institute. All animal procedures complied with protocols approved by the Johns Hopkins Institutional Animal Care and Use Committee and with recommendations for the proper use and care of laboratory mice.

Cells. Resting and naïve Ova-specific CD8$^+$ T cells (OT-I) harvested from spleens of OT-I transgenic mice were employed. Cells were passaged weekly at 1:4 dilution and

stimulated with irradiated tumor cells (TC-1) pre-pulsed with Ova epitope (SIINFEKL). T cells were cultured in RPMI-1640 medium supplemented with 10% FBS.

Synthesis and purification of pMHC/ANXA5. The Kb(Ova)/ANXA5 protein is composed of the mouse $\beta 2$ microglobulin signal peptide at the N-terminus, SIINFEKL epitope, $(GGGGS)_3$ linker, mouse $\beta 2$ microglobulin, $(GGGGS)_4$ linker, and the α_1, α_2, α_3 H-2K^b heavy chain, followed by ANXA5. A 6× polyhistidine (his) tag was appended at the C-terminus to facilitate protein purification. The Kb(Ova) protein is identical to Kb(Ova)/ANXA5 except that it lacks the ANXA5 component. Plasmids encoding Kb(Ova)/ANXA5 or Kb(Ova) were generated by recombinant DNA technology and verified by DNA sequencing. Plasmids were transfected into suspension 293T cells; the encoded protein was subsequently purified by affinity chromatography on a nickel column and eluted with imidazole. Protein was then dialyzed and reconstituted in PBS. Protein integrity and purity were confirmed by SDS-PAGE. The predicted molecular weights of Kb(Ova)/ANXA5 and Kb(Ova) are 84 kD and 49 kD, respectively.

Verification of pMHC/ANXA5 protein. Liposomes of ~1 μm diameter containing nickel-NTA or PS were synthesized by lipid film hydration and membrane extrusion. To test pMHC display, Kb(Ova)/ANXA5 or Kb(Ova) protein (1 μg) was conjugated to nickel-NTA liposomes via the his tag and stained with PE-labeled α-H-2K^b/SIINFEKL antibody. Liposomes were examined by flow cytometry, with average PE fluorescence serving as an index of pMHC display. To test ANXA5 binding, Kb(Ova)/ANXA5 or Kb(Ova) protein (1 μg) was added to PS liposomes, stained with PE-labeled α-H-2K^b/SIINFEKL antibody, and interrogated by flow cytometry as described above.

Characterization of PS exposure on T cells. For *in vitro* experiments, resting OT-I T cells were incubated with SIINFEKL-loaded TC-1 feeder cells (1:1 ratio) for 72 hr. At 12, 24, 48, and 72 hr, cells were harvested, stained with FITC-labeled ANXA5, and examined by flow cytometry. The percentage of ANXA5$^+$ cells, as well as mean ANXA5 binding intensity, were ascertained. To test PS exposure in response to weak antigen stimuli, resting OT-I cells were treated with monomeric Kb(Ova) protein or Ova peptide (1 μg/ml), and ANXA5 binding was measured as described above. For *ex vivo* experiments, naïve splenocytes were extracted from C57BL/6 mice and pulsed overnight with plate-coated α-CD3 antibody (1 μg/ml). Cells were stained with fluorophore-labeled α-CD8 and α-CD69 antibody, as well as FITC-labeled ANXA5. Lymphocyte activation and ANXA5 binding were determined by flow cytometry as described above.

Characterization of lymphocyte activation. For *in vitro* experiments, T cells were seeded in 96-well plates at 10^4 cells/well and incubated with pMHC/ANXA5 in the presence of brefeldin A. After 12 hr, cells were harvested, stained for CD8, permeabilized, and stained for IFN-γ. Cells were examined by flow cytometry, and IFN-γ expression was measured as an activation index. For *in vivo* experiments, spleens were harvested from mice at different time points after vaccination. Spleens were processed into single cells, stained for CD8 and IFN-γ, and interrogated by flow cytometry as described above.

***In vivo* vaccination.** For early lymphocyte activation experiments, OT-I transgenic mice received 20 μg of Kb(Ova) or Kb(Ova)/ANXA5 via intravenous injection. Splenocytes were harvested the following day for analysis. For vaccination experiments, C57BL/6 or 232-4 transgenic mice received protein (20 μg) via subcutaneous injection twice at a 7-day interval. After two weeks, splenocytes were removed for analysis. For

lymphocyte proliferation experiments, C57BL/6 mice were adoptively transferred CFSE-labeled OT-I cells (10^6 per animal) by intravenous injection. After one day, mice received protein (ranging from 0.1-10 μg) via intravenous injection. On day five, PBMCs were collected and assessed for CFSE dilution by flow cytometry.

Altered peptide ligands (APLs). Single amino acid substitutions in the SIINFEKL (N4) peptide of Kb(Ova)/ANXA5 were generated by recombinant DNA technology to mimic low affinity pMHC-TCR interactions. Constructs were verified by DNA sequencing. The altered encoded peptide epitopes were: SIYNFEKL (Y3), SIIQFEKL (Q4), and SIITFEKL (T4). pMHC/ANXA5 containing APLs were incubated with resting OT-I cells for lymphocyte activation experiments as described above.

Synthesis of ANXA5 mutants. Amino acid substitutions were introduced in the calcium-binding domain of ANXA5 in pMHC/ANXA5 to disrupt PS binding: D144N and E228Q (mt136) or D144N, E228Q, and D303N (mt137) by recombinant DNA technology. To abolish ANXA5 aggregation, an altered ANXA5 molecule bearing five substitutions in the self-assembly domain was generated: R16E, R23E, K27E, K56E, K191E (mt5). Constructs were confirmed by DNA sequencing, and structural or functional alterations in the encoded protein were verified by SDS-PAGE as well as the liposome-based assays described above.

Single-molecule epifluorescence microscopy. Kb(Ova)/ANXA5 or Kb(Ova) protein was mixed with PE-labeled α-his tag antibody for 30 min and then added to resting OT-I cells pre-seeded at 300 cells/mm^2. Cells were incubated at 37°C for 5 hr, washed, and visualized by single-molecule epifluorescence microscopy to detect pMHC/TCR clustering.

Statistical analysis. All data in this study are presented as mean ± standard deviation (SD) and are representative of at least three independent experiments performed. Individual data points from flow cytometry results were evaluated by Student's t-test. P-values<0.05 were considered significant.

Figures
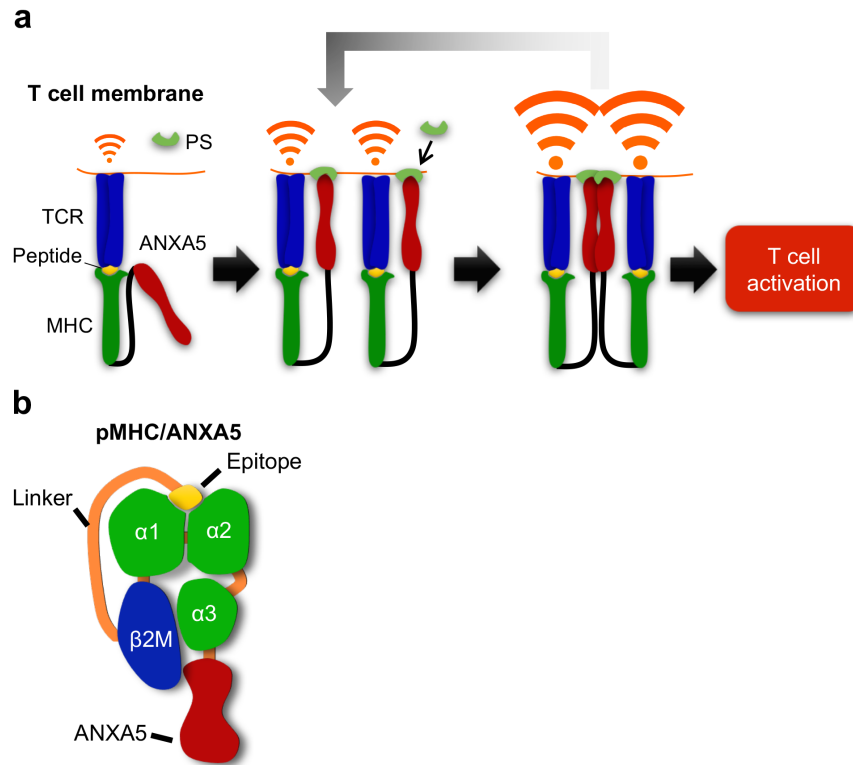
Figure II-1. Schematic diagram of the pMHC/ANXA5 system concept.

(**a**) Phosphatidylserine (PS) exposure upon cognate pMHC-TCR interactions is exploited to tether pMHC to the membrane via ANXA5, stabilizing pMHC-TCR binding and prompting TCR crosslinking. In this system, weak and transient pMHC-TCR encounters are converted into strong, repeated binding events by ANXA5, which induces further PS exposure in a positive feedback loop. Self-assembly of ANXA5 on the membrane facilitates TCR crosslinking and robust lymphocyte activation. (**b**) Model of the soluble pMHC/ANXA5 protein, composed of antigen epitope at the N-terminus linked to β2 microglobulin, MHC class I heavy chain, and ANXA5.
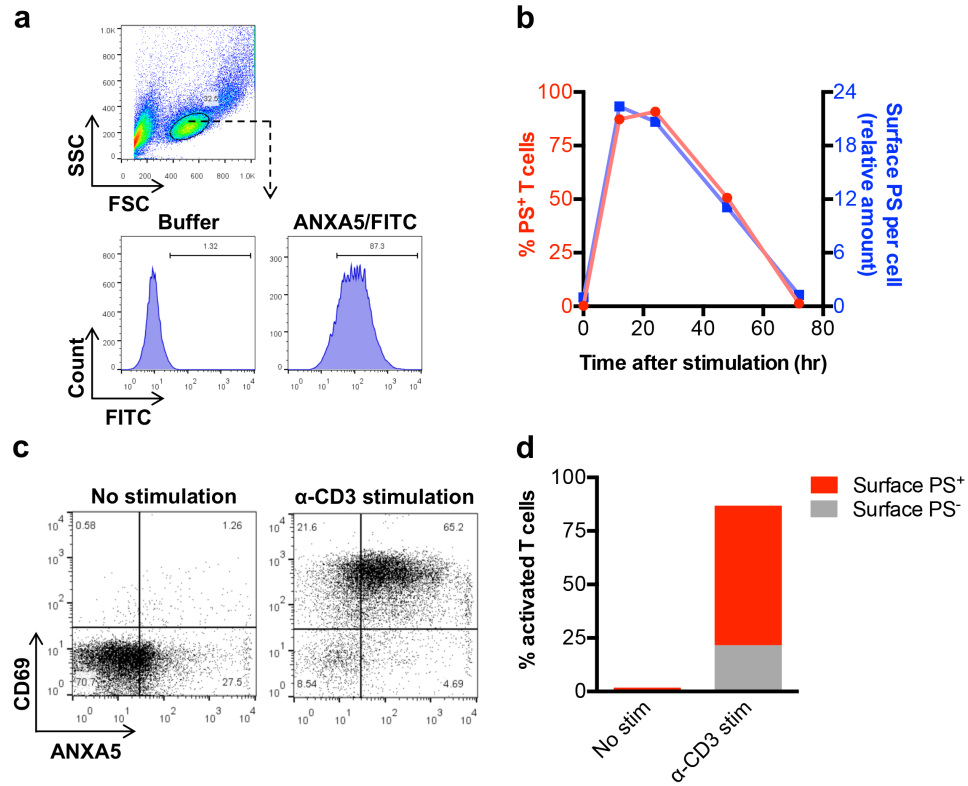
Figure II-2. Phosphatidylserine (PS) exposure on cognate T cells upon antigen stimulation.

(**a**) PS exposure on OT-I cells pulsed with SIINFEKL-loaded feeder cells for 12 hr. Cells were stained with FITC-labeled ANXA5 or buffer control and examined by flow cytometry. Live, activated T cells were gated by FSC/SSC profile (dot plot, top), and fluorescence was measured (histograms, bottom). (**b**) Kinetics of PS exposure on resting OT-I cells pulsed with peptide. (**c**) PS exposure on naïve splenocytes incubated with plate-coated α-CD3 antibody for 12 hr. Splenocytes were stained with fluorophore-labeled CD8, CD69, and ANXA5 antibodies. CD8^{+} T cells were gated by FSC/SSC profile and CD8 expression, and the distribution of CD69^{+} and/or ANXA5^{+} cells is shown in the dot plots. (**d**) Quantification of PS exposure on naïve splenocytes with or without α-CD3 stimulation. Activation of splenocytes was measured by CD69 expression. Data are representative of results from at least three independent experiments.
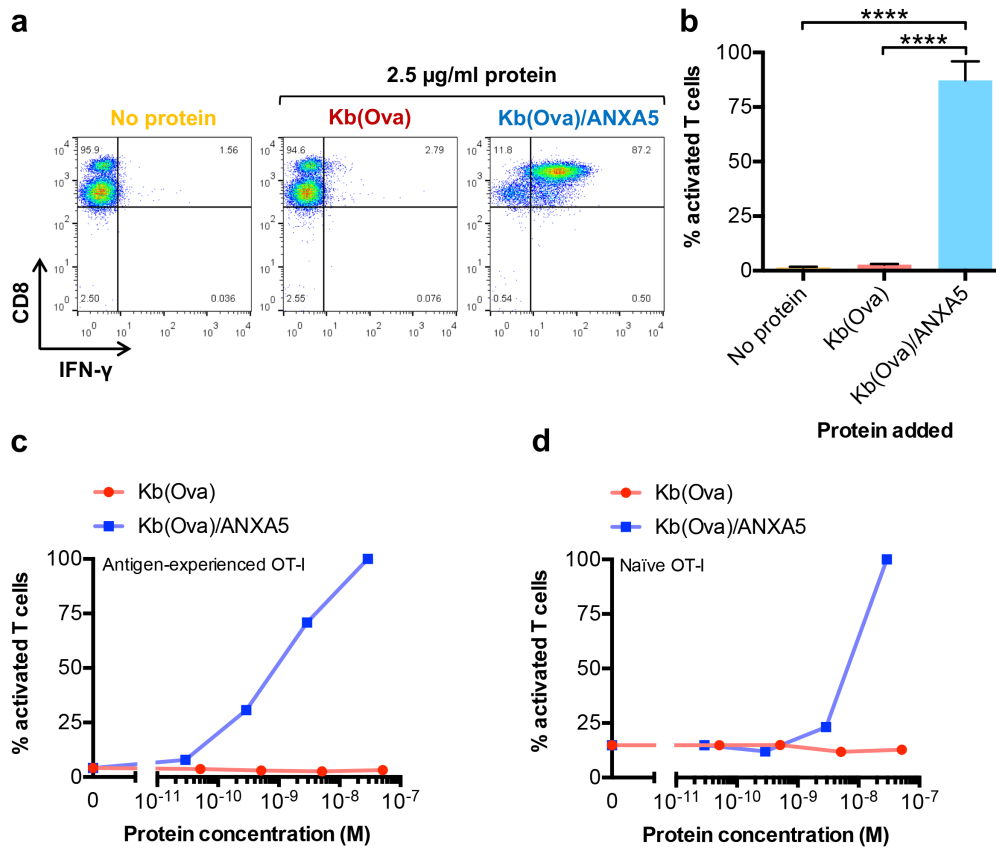
Figure II-3. Lymphocyte activation by pMHC/ANXA5.

(**a**) Resting OT-I cells were incubated for 12 hr with Kb(Ova) or Kb(Ova)/ANXA5 at 2.5 µg/ml in the presence of brefeldin A. Activation of $CD8^+$ T cells was determined by flow cytometry analysis of IFN-γ expression. (**b**) Bar graph quantification of lymphocyte activation frequency (*n*=3). (**c**) Resting OT-I cells or (**d**) splenic T cells harvested freshly from OT-I transgenic mice were incubated for 12 hr with Kb(Ova) or Kb(Ova)/ANXA5 at various molar concentrations. Activation of T cells was determined by flow cytometry analysis of IFN-γ expression. Data are representative of results from at least three independent experiments. Data are presented as mean±SD. ****$P<0.0001$.
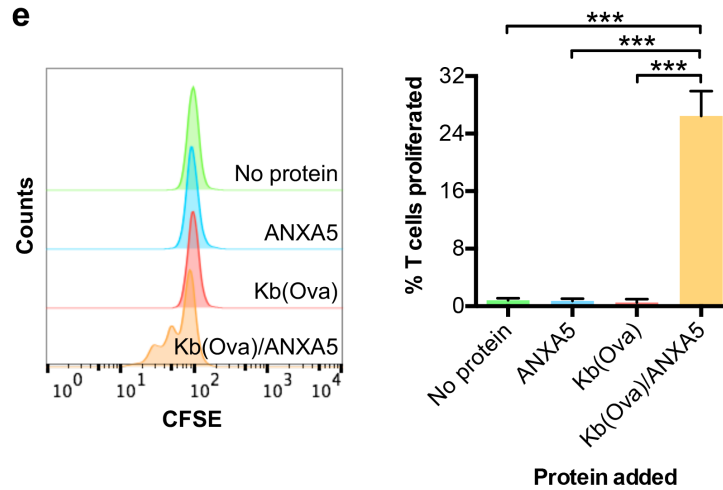
Figure II-3 (continued). Lymphocyte activation by pMHC/ANXA5. (**e**) Proliferation of T cells by pMHC/ANXA5. Resting OT-I cells were labeled with CFSE and incubated with ANXA5, Kb(Ova), or Kb(Ova)/ANXA5. Proliferation was measured after three days based on CFSE dilution. Histograms (left) display CFSE intensity and bar graph (right) depicts the frequency of T cells that underwent proliferation (*n=3*). Data are representative of results from at least three independent experiments. Data are presented as mean±SD. ****P*<0.001.
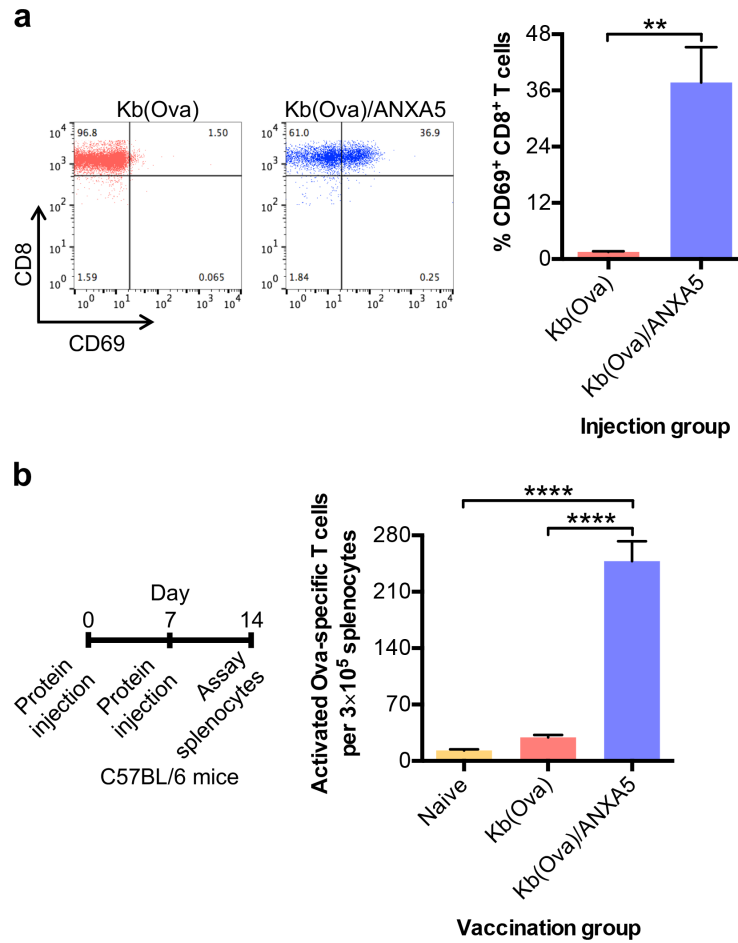
Figure II-4. In vivo activation of antigen-specific T cells by pMHC/ANXA5.

(**a**) Early costimulation-independent lymphocyte activation by pMHC/ANXA5. OT-I transgenic mice were administered Kb(Ova) or Kb(Ova)/ANXA5, and the percentage of $CD69^+CD8^+$ T cells was measured after one day by flow cytometry. Left: representative dot plots, right: bar graph quantification (*n*=3 mice per group). (**b**) Amplification of rare antigen-specific lymphocyte precursors by pMHC/ANXA5. C57BL/6 mice were administered Kb(Ova) or Kb(Ova)/ANXA5, and activation of Ova-specific $CD8^+$ T cells was assessed after two weeks based on IFN-γ expression. Left: experiment timeline, right: bar graph depicting frequency of lymphocyte precursors post-vaccination (*n*=5 mice per group). Data are presented as mean±SD. **P<0.01, ****P<0.0001.

c

Kb(Ova)
Kb(Ova)/ANXA5

Injection group	EC$_{50}$ (pmol protein)
Kb(Ova)	61.8
Kb(Ova)/ANXA5	0.59

Day

0 1   5

OT-I transfer
Protein injection

Assay PBMCs

% T cells proliferated

Protein dose (mol)

d

Day

0   7   14

Protein injection
Protein injection
Assay splenocytes

232-4 transgenic mice

Ova-specific IFN-γ^+ CD8$^+$ T cells per 3×10^5 splenocytes

(+) SIINFEKL
(−) SIINFEKL

Detection limit

Naïve   Kb(Ova)   Kb(Ova)/ANXA5
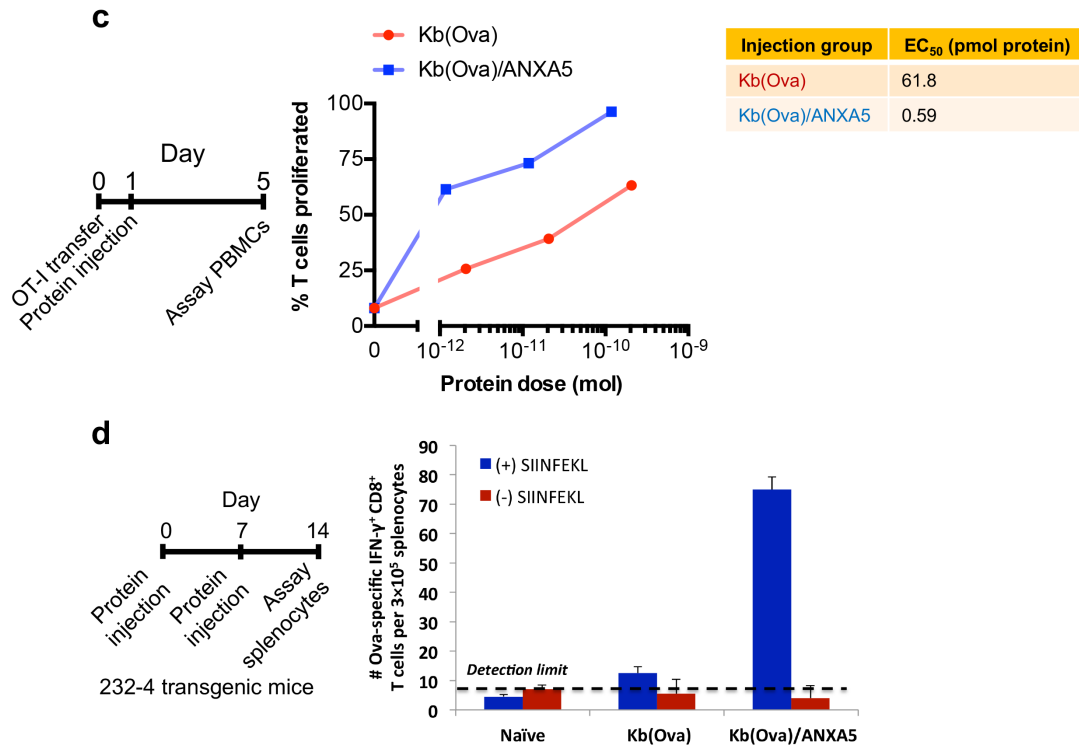
Figure II-4 (continued). In vivo activation of antigen-specific T cells by pMHC/ANXA5. (**c**) Proliferation of systemic cognate T cells by pMHC/ANXA5. CFSE-labeled OT-I cells were adoptively transferred into C57BL/6 mice (*n*=5 mice per group), followed by Kb(Ova) or Kb(Ova)/ANXA5 infusion. Lymphocyte proliferation was monitored by CFSE dilution. Left: experiment timeline, right: proliferation index. EC$_{50,}$ minimum injection dose needed to elicit 50% proliferation. (**d**) Reversal of immune tolerance to self-antigen by pMHC/ANXA5. Transgenic 232-4 mice with ectopic expression of Ova antigen in the intestine were administered with either Kb(Ova) or Kb(Ova)/ANXA5 by subcutaneous injection. The frequency of IFN-γ^+ CD8$^+$ T cells was determined by flow cytometry. Left: experiment timeline, right: bar graph quantification of lymphocyte activation.

37
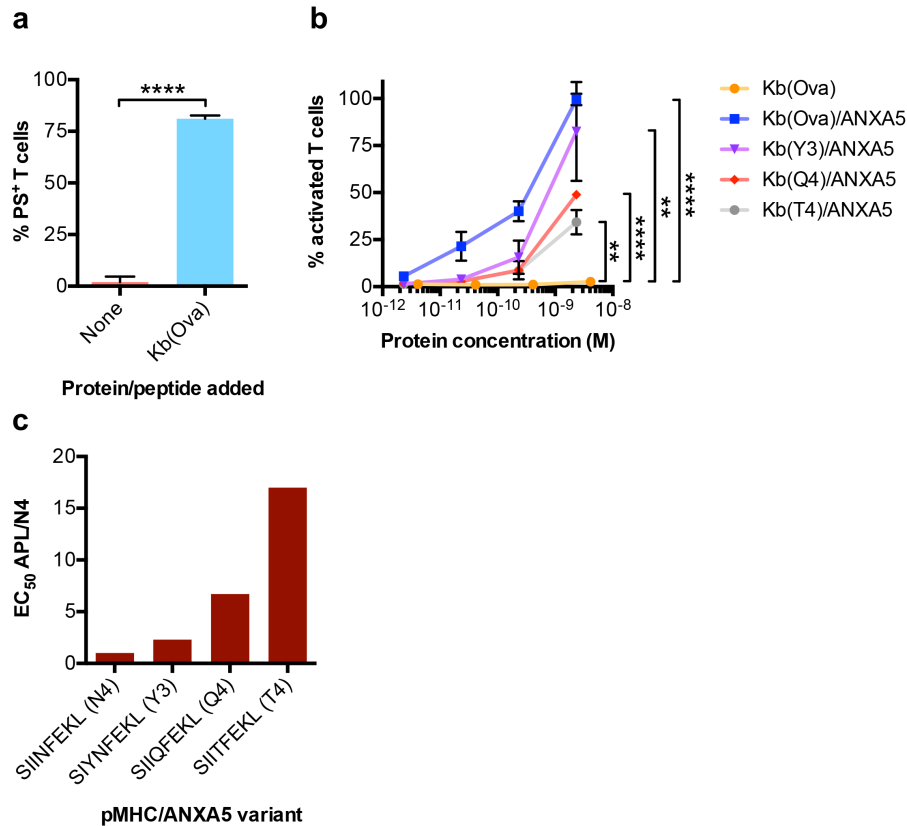
Figure II-5. Reversal of low-affinity pMHC-TCR interactions by ANXA5 fusion to pMHC.
 (**a**) Phosphatidylserine (PS) exposure on cognate T cells in response to weak antigen stimuli. OT-I cells were incubated with monomeric Kb(Ova) protein. Cells were stained after one day with FITC-labeled ANXA5, and the frequency of PS$^+$ T cells was measured one day later by flow cytometry. Bar graph depicts frequency of PS$^+$ cells (*n*=3). (**b, c**) Lymphocyte activation by pMHC/ANXA5 in the context of low affinity pMHC-TCR interactions. ANXA5-linked altered peptide ligands carrying indicated single amino acid substitutions in the SIINFEKL epitope were incubated with OT-I cells. (**b**) The frequency of IFN-γ^+ T cells was quantified (*n*=3). (**c**) Bar graph depicting the ratio of the amount of pMHC/ANXA5 protein, with wildtype or mutant Ova epitopes, needed to prime 50% of T cells (EC$_{50}$). Data are representative of results from at least three independent experiments and presented as mean±SD. ******$P<0.01$, ********$P<0.0001$.
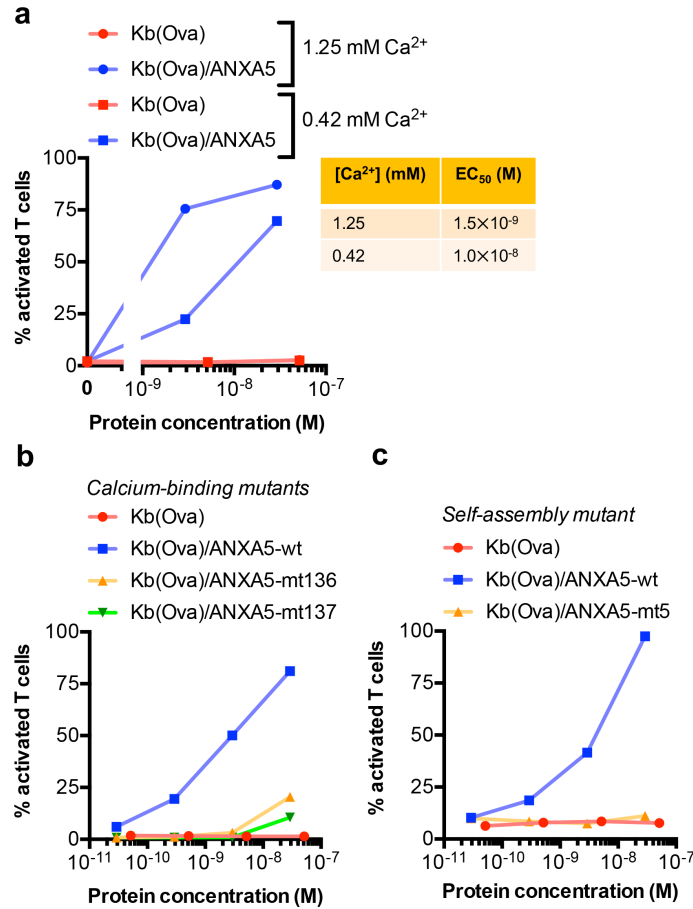
Figure II-6. Mechanisms underlying lymphocyte activation by pMHC/ANXA5.

(**a**) Calcium dependence of lymphocyte activation by pMHC/ANXA5. T cells were incubated for 12 hr with Kb(Ova) or Kb(Ova)/ANXA5 in medium containing different calcium concentrations. Lymphocyte activation was determined based on IFN-γ expression. EC_{50}, minimum protein amount needed to reach 50% activation. (**b, c**) Effect of structural ANXA5 mutations on lymphocyte activation by pMHC/ANXA5. Kb(Ova)/ANXA5 carrying mutations that disrupt either (**b**) the calcium-binding domain domain (D144N, E228Q (mt136) or D144N, E228Q, D303N (mt137)) or (**c**) the self-assembly domain (R16E, R23E, K27E, K56E, K191E (mt5)) were for 12 hr with OT-I cells. Lymphocyte activation was assessed by IFN-γ expression. Data are representative of results from at least three independent experiments.
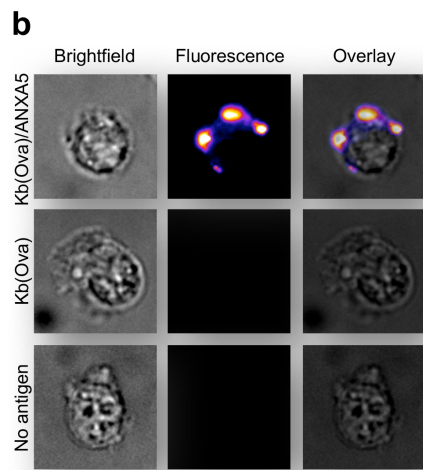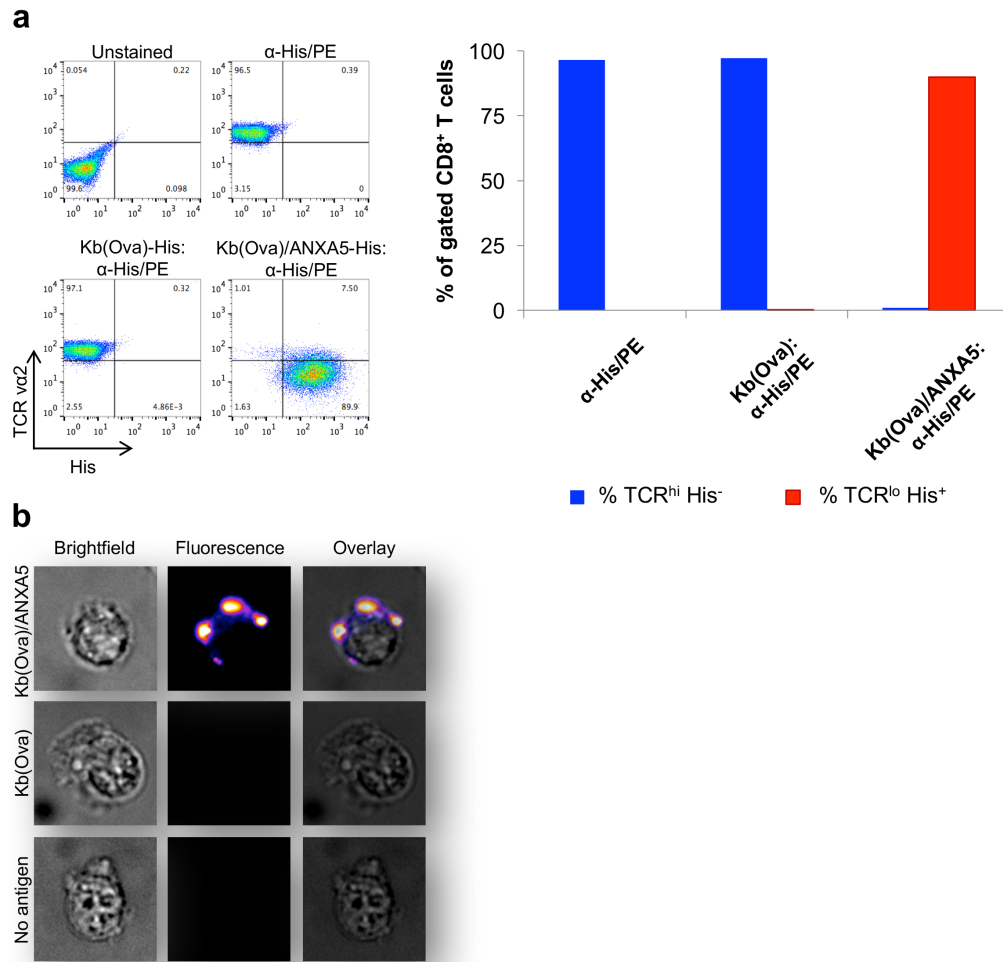
Figure II-7. Antigen membrane tethering, TCR crosslinking, and TCR downregulation mediated by pMHC/ANXA5.

His tag[+] Kb(Ova) or Kb(Ova)/ANXA5 was pre-mixed with PE-labeled α-his tag antibody and then incubated with low-density (~300 cells/mm^2 density) resting OT-I cells at 37°C for 5 hr. Cells were stained for CD8 and TCR (Vα2), and examined for fluorescence by flow cytometry. (**a**) Left: representative dot plots. Right: the percentage of T cells classified into indicated categories of TCR surface density and pMHC binding was quantified. (**b**) Cells were visualized by single-molecule epifluorescence microscopy. Representative imaging micrographs are shown. Data are representative of results from at least three independent experiments.
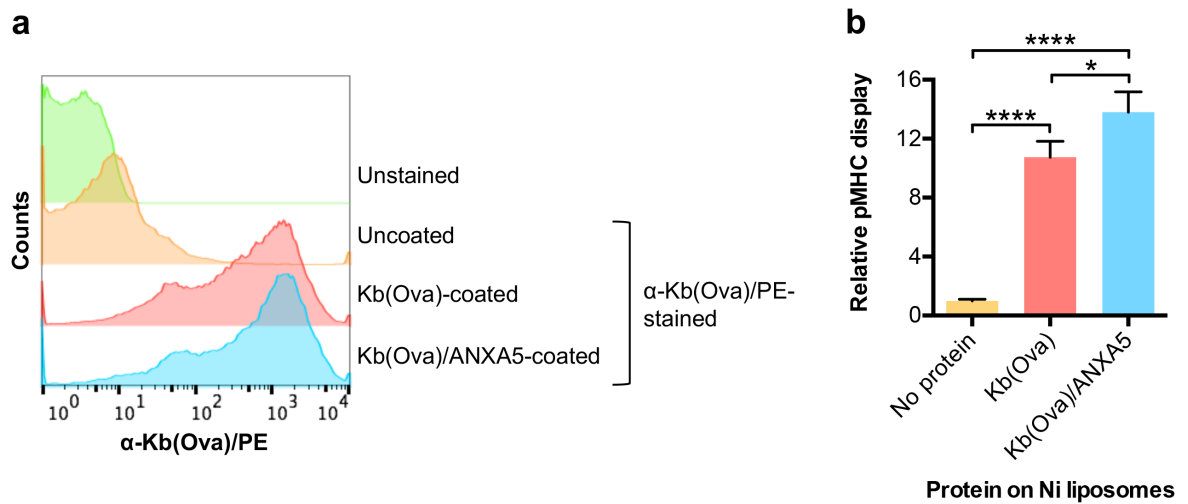
Supplementary Figure II-1. Validation of pMHC/ANXA5.

Ni-NTA liposomes were coated with Kb(Ova) or Kb(Ova)/ANXA5 protein (both bearing his tags) and then stained with α-H-2K^b-SIINFEKL antibody to verify peptide display. (**a**) Histogram and (**b**) bar graph depicting relative pMHC density on liposomes (*n*=3). Data are presented as mean±SD. *P<0.05, ****P<0.0001.
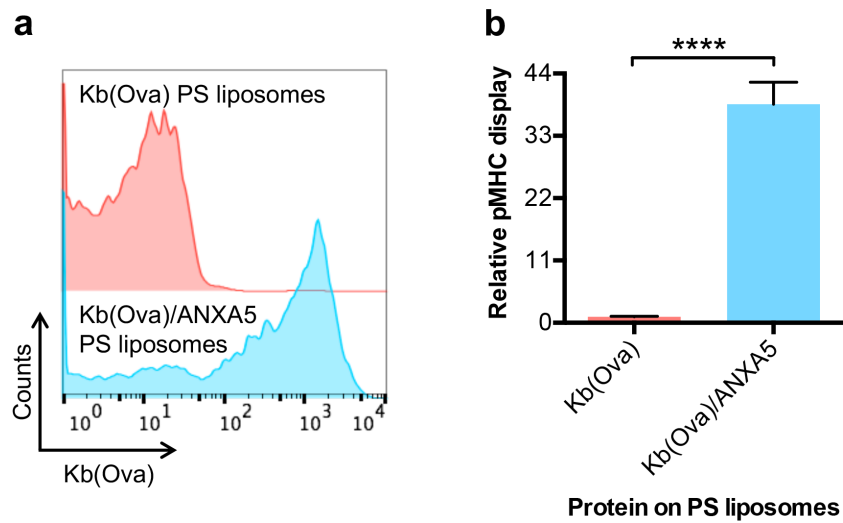
Supplementary Figure II-2. Assay of pMHC/ANXA5 binding to phosphatidylserine (PS). PS-containing liposomes were treated with Kb(Ova) or Kb(Ova)/ANXA5 and stained with α-H-2K^b-SIINFEKL antibody. (**a**) Histogram and (**b**) bar graph depicting relative pMHC density on PS liposomes (*n*=3). Data are presented as mean±SD. *****P*<0.0001.
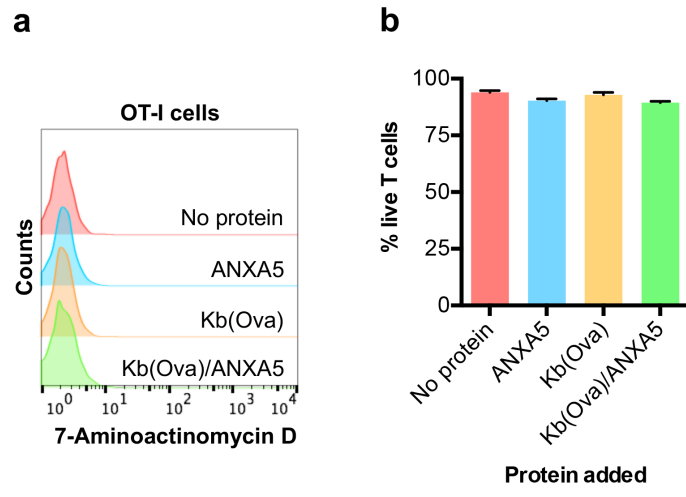
Supplementary Figure II-3. Viability of T cells treated with pMHC/ANXA5.

OT-I cells were incubated with indicated proteins. After three days, lymphocyte viability was assessed by 7-aminoactinomycin D (7-AAD) staining. (**a**) Histogram of 7-AAD intensity and (**b**) bar graph depicting the percentage of live cells in each group (n=3). Data are presented as mean±SD.
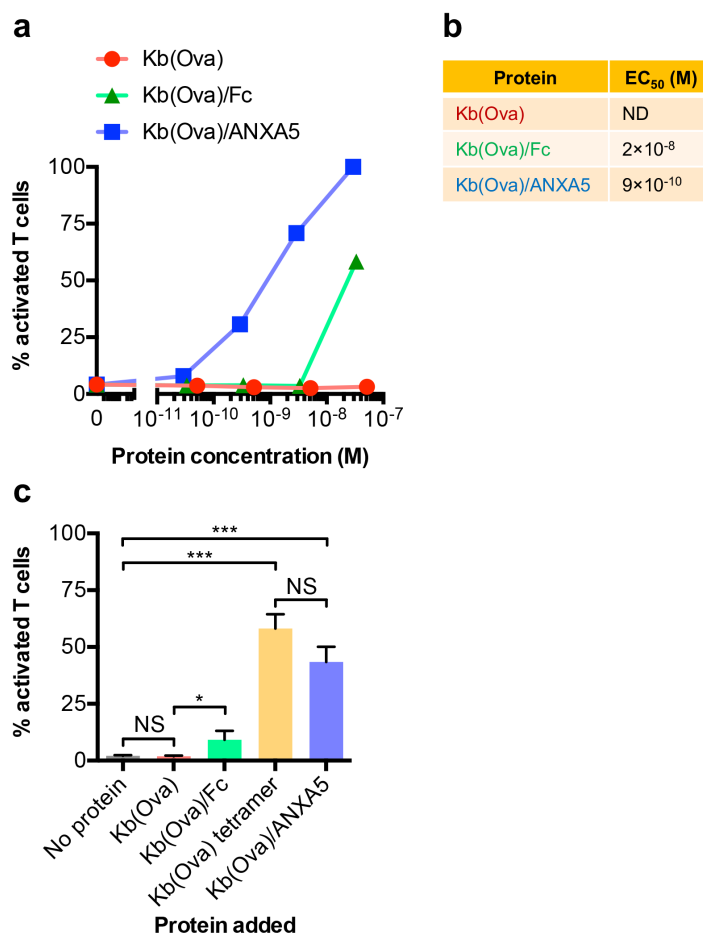
Supplementary Figure II-4. Comparison of lymphocyte activation by Kb(Ova)/ANXA5 to dimeric Kb(Ova)/Fc or tetrameric Kb(Ova).

Resting OT-I cells were incubated with indicated concentrations of Kb(Ova), Kb(Ova)/Fc, or tetrameric Kb(Ova). IFN-γ expression was measured as an index of lymphocyte activation. (**a**) Line graph depicting the percentage of IFN-γ^+ T cells at different Kb(Ova), Kb(Ova)/ANXA5, or Kb(Ova)/Fc concentrations. (**b**) Table of EC$_{50}$ values, defined as the minimum protein amount required for 50% activation. (**c**) Bar graph depicting the percentage of IFN-γ^+ T cells at 2.5 μg/ml Kb(Ova)/ANXA5 or tetrameric Kb(Ova) (*n*=3). Data are presented as mean±SD. *$P<0.05$, ***$P<0.001$, NS, not significant.
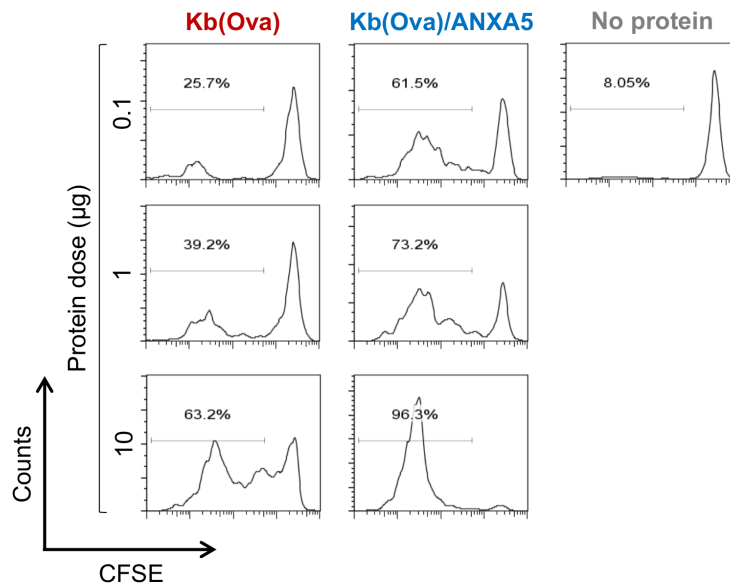
Supplementary Figure II-5. Proliferation of systemic cognate T cells by pMHC/ANXA5.
CFSE-labeled OT-I cells were transferred into C57BL/6 mice, followed by Kb(Ova) or Kb(Ova)/ANXA5 infusion at various doses. Lymphocyte proliferation was monitored by CFSE dilution. Representative histograms display CFSE intensity in each injection group.
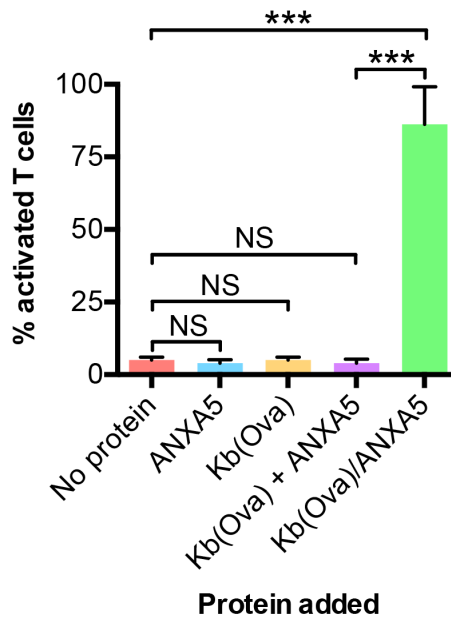
Supplementary Figure II-6. Requirement for pMHC-ANXA5 fusion for lymphocyte activation by the dynamic anchor.

Resting OT-I cells were incubated for 12 hr with ANXA5, Kb(Ova), combined ANXA5 and Kb(Ova), or Kb(Ova)/ANXA5 fusion protein. Lymphocyte activation was measured by IFN-γ expression (*n*=3). Data are presented as mean±SD. ***P<0.001, NS, not significant.
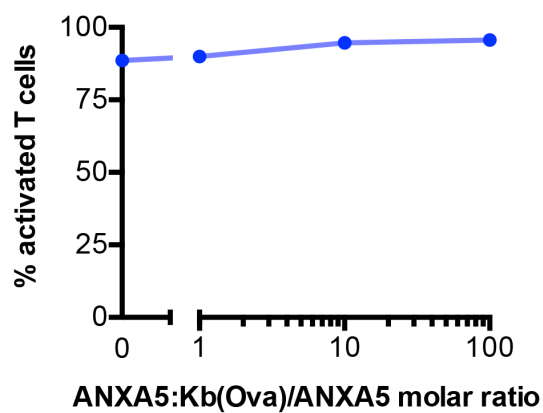
Supplementary Figure II-7. Lymphocyte activation by pMHC/ANXA5 in the presence of excess ANXA5.

Resting OT-I cells were incubated for 12 hr with a mixture of Kb(Ova)/ANXA5 and ANXA5 at various molar ratios (from 1:1 to 1:00). Lymphocyte activation was measured by IFN-γ expression. Data are representative results from three independent experiments.

References

1.   Galon, J. et al. Type, density, and location of immune cells within human colorectal tumors predict clinical outcome. *Science* **313**, 1960-1964 (2006).

2.   Grivennikov, S.I., Greten, F.R. & Karin, M. Immunity, inflammation, and cancer. *Cell* **140**, 883-899 (2010).

3.   Laghi, L. et al. CD3+ cells at the invasive margin of deeply invading (pT3-T4) colorectal cancer and risk of post-surgical metastasis: a longitudinal study. *The Lancet. Oncology* **10**, 877-884 (2009).

4.   Swann, J.B. & Smyth, M.J. Immune surveillance of tumors. *The Journal of clinical investigation* **117**, 1137-1146 (2007).

5.   Zhang, L. et al. Intratumoral T cells, recurrence, and survival in epithelial ovarian cancer. *The New England journal of medicine* **348**, 203-213 (2003).

6.   Mueller, D.L. Mechanisms maintaining peripheral tolerance. *Nature immunology* **11**, 21-27 (2010).

7.   Starr, T.K., Jameson, S.C. & Hogquist, K.A. Positive and negative selection of T cells. *Annual review of immunology* **21**, 139-176 (2003).

8.   Gonzalez, P.A. et al. T cell receptor binding kinetics required for T cell activation depend on the density of cognate ligand on the antigen-presenting cell. *Proceedings of the National Academy of Sciences of the United States of America* **102**, 4824-4829 (2005).

9.   Holler, P.D. & Kranz, D.M. Quantitative analysis of the contribution of TCR/pepMHC affinity and CD8 to T cell activation. *Immunity* **18**, 255-264 (2003).

10. Xie, J. et al. Photocrosslinkable pMHC monomers stain T cells specifically and cause ligand-bound TCRs to be 'preferentially' transported to the cSMAC. *Nature immunology* **13**, 674-680 (2012).

11. Huang, J. et al. The kinetics of two-dimensional TCR and pMHC interactions determine T-cell responsiveness. *Nature* **464**, 932-936 (2010).

12. Huppa, J.B. et al. TCR-peptide-MHC interactions in situ show accelerated kinetics and increased affinity. *Nature* **463**, 963-967 (2010).

13. Valitutti, S., Muller, S., Cella, M., Padovan, E. & Lanzavecchia, A. Serial triggering of many T-cell receptors by a few peptide-MHC complexes. *Nature* **375**, 148-151 (1995).

14. Boniface, J.J. et al. Initiation of signal transduction through the T cell receptor requires the multivalent engagement of peptide/MHC ligands [corrected]. *Immunity* **9**, 459-466 (1998).

15. Fahmy, T.M., Bieler, J.G., Edidin, M. & Schneck, J.P. Increased TCR avidity after T cell activation: a mechanism for sensing low-density antigen. *Immunity* **14**, 135-143 (2001).

16. Gerke, V., Creutz, C.E. & Moss, S.E. Annexins: linking Ca2+ signalling to membrane dynamics. *Nature reviews. Molecular cell biology* **6**, 449-461 (2005).

17. Hamad, A.R. et al. Potent T cell activation with dimeric peptide-major histocompatibility complex class II ligand: the role of CD4 coreceptor. *The Journal of experimental medicine* **188**, 1633-1640 (1998).

18. Vezys, V., Olson, S. & Lefrancois, L. Expression of intestine-specific antigen reveals novel pathways of CD8 T cell tolerance induction. *Immunity* **12**, 505-514 (2000).

19. Zehn, D., Lee, S.Y. & Bevan, M.J. Complete but curtailed T-cell response to very low-affinity antigen. *Nature* **458**, 211-214 (2009).

20. Jin, M., Smith, C., Hsieh, H.Y., Gibson, D.F. & Tait, J.F. Essential role of B-helix calcium binding sites in annexin V-membrane binding. *The Journal of biological chemistry* **279**, 40351-40357 (2004).

21. Bouter, A. et al. Annexin-A5 assembled into two-dimensional arrays promotes cell membrane repair. *Nature communications* **2**, 270 (2011).

22. Cai, Z. et al. Requirements for peptide-induced T cell receptor downregulation on naive CD8+ T cells. *The Journal of experimental medicine* **185**, 641-651 (1997).

23. Makkouk, A. & Weiner, G.J. Cancer immunotherapy and breaking immune tolerance: new approaches to an old challenge. *Cancer Res* **75**, 5-10 (2015).

24. Chen, L. & Flies, D.B. Molecular mechanisms of T cell co-stimulation and co-inhibition. *Nat Rev Immunol* **13**, 227-242 (2013).

25. Zou, W. Immunosuppressive networks in the tumour environment and their therapeutic relevance. *Nat Rev Cancer* **5**, 263-274 (2005).

26. Palucka, K. & Banchereau, J. Cancer immunotherapy via dendritic cells. *Nat Rev Cancer* **12**, 265-277 (2012).

27. Wang, B., Maile, R., Greenwood, R., Collins, E.J. & Frelinger, J.A. Naive CD8+ T cells do not require costimulation for proliferation and differentiation into cytotoxic effector cells. *Journal of immunology* **164**, 1216-1222 (2000).

28.   Gubin, M.M. et al. Checkpoint blockade cancer immunotherapy targets tumour-specific mutant antigens. *Nature* **515**, 577-581 (2014).

29.   Linnemann, C. et al. High-throughput epitope discovery reveals frequent recognition of neo-antigens by CD4+ T cells in human melanoma. *Nat Med* **21**, 81-85 (2015).

30.   Rizvi, N.A. et al. Cancer immunology. Mutational landscape determines sensitivity to PD-1 blockade in non-small cell lung cancer. *Science* **348**, 124-128 (2015).

31.   van Rooij, N. et al. Tumor exome analysis reveals neoantigen-specific T-cell reactivity in an ipilimumab-responsive melanoma. *J Clin Oncol* **31**, e439-442 (2013).

32.   Yarchoan, M., Johnson, B.A., 3rd, Lutz, E.R., Laheru, D.A. & Jaffee, E.M. Targeting neoantigens to augment antitumour immunity. *Nat Rev Cancer* **17**, 209-222 (2017).

33.   Topalian, S.L., Drake, C.G. & Pardoll, D.M. Immune checkpoint blockade: a common denominator approach to cancer therapy. *Cancer Cell* **27**, 450-461 (2015).

34.   Riedl, S. et al. In search of a novel target - phosphatidylserine exposed by non-apoptotic tumor cells and metastases of malignancies with poor treatment efficacy. *Biochim Biophys Acta* **1808**, 2638-2645 (2011).

35.   Ran, S. & Thorpe, P.E. Phosphatidylserine is a marker of tumor vasculature and a potential target for cancer imaging and therapy. *Int J Radiat Oncol Biol Phys* **54**, 1479-1484 (2002).

36. Utsugi, T., Schroit, A.J., Connor, J., Bucana, C.D. & Fidler, I.J. Elevated expression of phosphatidylserine in the outer membrane leaflet of human tumor cells and recognition by activated human blood monocytes. *Cancer Res* **51**, 3062-3066 (1991).

37. Piersma, S.J. et al. High number of intraepithelial CD8+ tumor-infiltrating lymphocytes is associated with the absence of lymph node metastases in patients with large early-stage cervical cancer. *Cancer Res* **67**, 354-361 (2007).

38. Dillon, S.R., Mancini, M., Rosen, A. & Schlissel, M.S. Annexin V binds to viable B cells and colocalizes with a marker of lipid rafts upon B cell receptor activation. *Journal of immunology* **164**, 1322-1332 (2000).

39. Elliott, J.I. et al. Phosphatidylserine exposure in B lymphocytes: a role for lipid packing. *Blood* **108**, 1611-1617 (2006).

III. Chapter 3. Single-molecule profiling of circulating mutant tumor proteins

Quantitative and structural analysis of circulating mutant tumor proteins may provide insight into disease in cancer patients. However, these proteins are rare in the circulation and therefore inaccessible to existing methods. We developed an imaging technology based on total internal reflection fluorescence microscopy in a microfluidic device to identify circulating mutant tumor proteins at single-molecule resolution and characterize their structural composition. As proof-of-principle, we focused on the p53 transcription factor, which is almost universally altered in human high-grade serous ovarian cancer[1]. Our technology identified the presence of mutant p53 in plasma from ovarian cancer patients and revealed that it aggregates into complexes of diverse size. Furthermore, single-molecule imaging discovered that patients who lacked circulating mutant p53 produced abundant anti-p53 autoantibodies, suggesting that host immune responses clear mutant tumor proteins from the blood. Structural analysis of circulating tumor proteins and their cognate autoantibodies introduces new possibilities for minimally invasive disease profiling.

Blood-based cancer detection, diagnosis, and monitoring currently centers around measurement of tumor biomarker levels[2]. Emergent techniques, such as digital ELISA[3], DNA biobarcoding[4-6], proximity ligation[7, 8], or immuno-PCR[9-11], have substantially lowered the detection limit of biomarker assays, often pushing sensitivity into the attomolar (aM) range[12]. However, strictly quantitative conventional biomarker measurement suffers

from limited specificity due to potential basal release of these proteins from non-transformed cells into the blood[2]. Also, existing methods do not yield information about structural features of tumor-derived proteins. Because mutant oncoproteins or tumor suppressor proteins are exclusive to tumor cells and frequently possess unique structural characteristics, we reasoned that the analysis of these characteristics would improve the specificity of disease detection, as well as shed light on biochemical features of a tumor that may be amenable to therapy.

To characterize structural features of circulating mutant tumor proteins, we developed an imaging technology based on single-molecule total internal reflection fluorescence microscopy (TIRFM). By interrogating individual proteins in space, TIRFM provides structural information about proteins that cannot be attained via standard ultra-sensitive assays. For instance, Ha and coworkers used single-molecule TIRFM to dissect the composition of various complexes of cytosolic, membrane, and organelle-associated proteins[13]. In addition, Lee *et al.* implemented this technique to investigate the kinetics of Ras signaling *in vitro*[14]. However, TIRFM-based methods have thus far not reached a detection limit below the pM (10^{-12} M) range, restricting their utility in the clinical setting[13, 15]. Indeed, TIRFM has not been previously applied to study proteins in clinical samples such as human blood. Here we report a TIRFM platform—which we call SiMSI (for Single-Molecule Structural Imaging)—that provides structural insight into proteins with single-molecule resolution at a sub-fM ($<10^{-15}$ M) concentration range, $>10^3$-fold below current TIRFM-based techniques. We applied SiMSI to profile rare mutant tumor proteins and their cognate autoantibodies in blood from cancer patients.

Our technology capitalizes on the principle of single-molecule pulldown[16] on a borosilicate surface passivated with a high-density mixture of 5 kD polyethylene glycol (PEG) and a biotinylated PEG functional group[18], which serves as an attachment site for antibodies conjugated via a NeutrAvidin linker. To concentrate target protein in a 1.8 mm^2 region, we covalently assembled the surface to a microfluidic chamber (200 μm width × 200 μm height) patterned with a staggered herringbone micromixer[16] (**Figure III-1a**). We continuously passed samples at 500 μl/min in the chip to capture target protein with >100-fold greater efficiency over standard incubation (**Supplementary Figure III-1a, b**). We probed for target protein with fluorophore-labeled antibodies and applied a stringent wash regimen with 10^4-fold chip volume to confine background to <10 non-specific binding events per imaging area. We performed single-molecule TIRFM on the chip over a time stream of 500 frames with 50 ms exposure time. We set each imaging area at 625 μm^2 for a total of ~3,000 imaging regions per chip. For data analysis, we applied a dynamic thresholding algorithm to digitally count the number of protein copies per imaging area and to localize protein complexes to 20-nm resolution (**Figure III-1a** and **Supplementary Figure III-2a, b**). We deduced the structural composition of complexes by inspecting fluorescence data with integrated Gaussian multiple emitter fitting analysis (**Figure III-1a**).

We first evaluated SiMSI using GFP as a reporter protein. We detected down to <500 aM (10^{-18} M) GFP (**Figure III-1b**), which corresponds to >50% capture efficiency. In general, this system attains >10% capture efficiency with antibodies of K_D~10^{-9} M affinity. Within the aM to pM range, molecule counts scaled linearly with target concentration (R^2=0.9987) (**Figure III-1b**). For imaging convenience, we maintained a

capture area of 1.8 mm^2 in this study, although we have observed that shrinking this area further augments sensitivity. At this chip size, our technology displays a sensitivity 10^4-fold greater than ELISA (**Figure III-1b**) and >10^3-fold superior to that previously achieved by single-molecule TIRFM[13, 15]. Since a fraction of GFP naturally dimerizes[17, 18], to validate SiMSI for structural analysis we examined the fluorescence distribution of this protein in its native state. As expected, GFP singlets emitted half the median intensity of doublets (**Supplementary Figure III-3a, b**). Based on these intensity values, we calculated the number of protein copies per imaging spot. Even at sub-fM concentrations, SiMSI could profile the size distribution of native protein with high resolution (**Figure III-1c, d**). This type of structural analysis has not been previously realized for such low amounts of target protein.

To illustrate the application of SiMSI to circulating tumor molecule structural analysis, we conducted proof-of-principle experiments in preclinical models to profile rare cytoplasmic proteins shed from tumor cells into the blood. Notably, almost all existing cancer biomarker assays measure membrane-associated or secreted proteins[19], and circulating cytoplasmic tumor-derived proteins (including mutant proteins) have not been rigorously explored. In mice with tumor cells carrying a cytoplasmic GFP reporter, SiMSI (but not ELISA) readily detected circulating GFP (>100-fold above background) within days after tumor challenge (**Figure III-1e**). The high sensitivity of this technology permitted us to study the kinetics and mechanism by which cytoplasmic tumor proteins enter the blood. We induced spontaneous tumor formation in mice by *in vivo* oncogene delivery[20], with cytoplasmic GFP and luciferase acting as tracers of tumor progression (**Supplementary Figure III-4**). Intriguingly, circulating GFP release was only observed

with concomitant oncogene (*Ras, Akt*) delivery (**Supplementary Figure III-5, 6**), implying that transformation instigates the release of cytoplasmic proteins from cells. Single-molecule imaging revealed that circulating cytoplasmic tumor proteins but not DNA emerge around one month after oncogenesis (before a tumor was visible on luminescence imaging) (**Figure III-1f** and **Supplementary Figure III-7, 8**), and accumulated with progressive tumor burden (**Figure III-1g**). By single-molecule structural analysis, we found that circulating GFP load correlated with formation of serum complexes (**Figure III-1h**), suggesting that a high density of cytoplasmic tumor proteins promotes their aggregation in the blood. Collectively, these results establish that SiMSI is able to identify and profile structural features of rare cytoplasmic proteins shed from tumor cells into the blood.

Since transformed cells release their contents into the blood via an oncogene-driven process, we reasoned that mutant tumor proteins, such as mutant Ras, may appear in the blood as well. We detected circulating Ras at ~100-fold higher levels in serum from mice bearing tumor cells with mutant compared to wildtype Ras independent of tumor growth rates (**Figure III-2a**), suggesting that mutant Ras facilitates its own export into the blood. As Ras has been shown to polymerize on the plasma membrane into transient nanoclusters[21], we observed these nanoclusters by SiMSI (**Figure III-2b, c**). In tumor-bearing mice, 1-4% of circulating mutant Ras (but not wildtype Ras) formed nanoclusters (**Figure III-2d, e**). Our data signify that circulating mutant Ras oncoproteins present an attractive target for cancer detection because they selectively enter the blood and are specific for transformed cells. To this end, we developed a preliminary SiMSI system that preferentially recognizes Ras[G12V] and Ras[G12D] (**Figure III-2f**), the variants that occur most

frequently in human cancer[22]. We are currently optimizing this system for clinical translation.

To build on the concept of circulating mutant protein detection, we next focused on the transcription factor p53. 96% of high-grade serous ovarian cancer cases carry mutant p53[1]. Moreover, while the proteasome rapidly degrades wildtype p53, mutant p53 evades the proteasome and accumulates within tumor cells[23, 24]. By SiMSI we detected <10 fM mutant p53 (R^2=0.9552), 10^4-fold below the ELISA limit (R^2=0.9939) (**Figure III-2g**). Furthermore, SiMSI detected p53 from cancer cells carrying multiple different p53 amino acid substitutions, but not from cells carrying wildtype p53 (**Figure III-2h**), indicating that this system is specific for mutant p53, likely due to stabilization of the mutant protein.

We applied SiMSI to characterize structural aspects of mutant p53. Conformational alterations in mutant p53 cause this transcription factor to precipitate into large complexes, a property that fosters oncogenesis[25, 26]. Thus, we verified this system in cells transfected with GFP-linked wildtype p53 or mutant p53 variants that either aggregate into large complexes (p53[R175H]) or fail to aggregate (p53[L344P])[25, 26] (**Figure III-2i-k** and **Supplementary Figure III-9, 10**). In cells with p53[R175H] (but not p53[L344P] or wildtype p53), we observed distinct imaging peaks corresponding to p53 tetramer, octamer, and large (>10-mer) complexes (**Figure III-2i-k**). We applied this system to investigate mutant p53 shed from cancer cells into the surrounding milieu. We detected non-vesicular mutant p53 release from as few as 10^3 human ovarian cancer cells (OVCAR3; *p53[R248Q]*) within 24 hr (**Figure III-2l, Supplementary Figure III-11**). To explore the structural features of mutant p53 before and after release from human cancer cells, we mapped the size distribution of mutant p53 in the nucleus, cytoplasm, and supernatant (**Figure III-2m,**

Supplementary Figure III-12a, b). As mutant p53 transitioned from nucleus to supernatant, complexes became remarkably diverse in size and on average ~30% smaller (**Figure III-2m**), implying that mutant p53 complexes partly dissociate during release. We implemented SiMSI to identify circulating mutant p53 early in tumor progression and to monitor disease dissemination in preclinical spontaneous tumor models (**Figure III-2n** and **Supplementary Figure III-13-16**). Together, these data highlight the utility of SiMSI in characterizing the structural composition of rare circulating mutant p53 complexes.

We therefore applied this technology to profile circulating mutant p53 in cancer patients. We verified that this system maintains a sensitivity of ~10 fM p53 in human plasma (R^2=0.9017) with negligible background across multiple subjects (**Figure III-3a** and **Supplementary Figure III-17, 18**). Structural analysis also indicated that mutant p53 complexes remain stable in human plasma (**Figure III-3b-d**). To profile structural properties of endogenous circulating mutant p53, we ascertained the fluorescence pattern of anti-p53 probe monoclonal antibodies, which split into distinct populations due to variation in dye labeling ratios (R^2=0.9874) (**Figure III-3e, f**). We used this data to project the number of proteins within mutant or wildtype p53 complexes (**Figure III-3g**).

By quantifying circulating p53 complexes, we detected circulating mutant p53 in ~50% of high-grade serous ovarian cancer patients (**Figure III-3h**); patients were confirmed to have tumor tissue p53 by immunohistochemistry. Moreover, healthy control subjects lacked circulating mutant p53 (**Figure III-3h**). We examined structural features of circulating mutant p53 in two patients by SiMSI and found that it polymerized into complexes of diverse size, with an average of 17.3±8.1 and 24.2±12.0 p53 copies/aggregate (**Figure III-3i, j** and **Supplementary Figure III-20**). The mutant p53 profile in these

patients differed conspicuously from background plasma signal in healthy subjects (**Figure III-3i, j** and **Supplementary Figure III-20**). Our results insinuate that these patients may harbor mutant p53 with conformational anomalies and underscore the power of single-molecule imaging to trace these structural alterations in a minimally invasive manner.

We reasoned that in patients who lacked circulating mutant p53, this protein may be depleted from the blood by host autoantibodies[27]. Since ELISA-based methods potentially miss autoantibodies in many patients, we developed a single-molecule assay for circulating anti-p53 autoantibodies, which performed with $>10^3$-fold superior sensitivity over ELISA (**Figure III-3k**). In a subset of our initial cohort of ovarian cancer patients, anti-p53 autoantibodies were markedly amplified as assessed by SiMSI (**Figure III-3l** and **Supplementary Figure III-21**). Remarkably, most patients with abundant p53 autoantibodies lacked circulating mutant p53, suggesting that host immune responses clear mutant tumor antigens from the blood. Overall, we detected circulating mutant p53 or amplified anti-p53 autoantibodies in ~80% (11 of 14) of ovarian cancer patients and in 0% (0 of 11) of control subjects (**Figure III-3m**). Thus, we conclude that the presence of circulating mutant proteins and their cognate autoantibodies are complementary, though not mutually exclusive, events in human cancer. These results warrant large-cohort studies employing single-molecule imaging to simultaneously characterize circulating mutant tumor proteins and their autoantibodies.

Altogether, we have shown that rare circulating mutant tumor proteins and their autoantibodies can be profiled by single-molecule imaging technology. We believe the structural and functional information to be garnered from this technology holds value, as it may shed light on the pathologic processes unfolding within the tumor of individual cancer

patients and point to effective management strategies. Thus, single-molecule profiling of mutant proteins and antibodies may be useful for cancer detection, diagnosis, and monitoring. Finally, this technology may also be applied to investigate other cancer-associated proteins that form complexes or different permutations of proteins within these complexes. For instance, Rodina *et al.* recently reported the concept of an 'epichaperome' of cancer, in which oncoproteins such as Myc rewire chaperone proteins, causing them to assemble into large complexes that promote cancer progression[28]. Intriguingly, emergence of the epichaperome occurs in a majority of cancer cases, and pharmacologic inhibition of the epichaperome impairs tumor survival[28]. Therefore, the structural analysis of these chaperone complexes, or other key tumor signaling machinery, in the blood might uncover new avenues for clinical intervention.

Methods

Materials. Polydimethylsiloxane (PDMS) elastomer for synthesis of SiMSI chips was purchased from Dow Corning. 22×22 mm borosilicate cover glass for the capture surface was from Fisher Scientific. Surface passivation relied on the following reagents: aminosilane (United Chemical Technologies), Alconox (Alconox, Inc.), methanol (Fisher Scientific), acetic acid (Sigma-Aldrich), sodium bicarbonate (Sigma-Aldrich), biotin-mPEG-succinimidyl valerate (biotin-mPEG-SVA) (Laysan Bio), and mPEG-SVA (Laysan Bio). Multiple anti-p53 antibodies were used, including: E47, Y5 (Abcam); 7F5 (Cell Signaling Technology); BAF1355 (R&D Systems); pAb240, DO-1, FL-393 (Santa Cruz Biotechnology); DO-7 (Thermo Scientific). For most applications in this study, BAF1355 was utilized for capture and E47 (C-terminus) or Y5 (N-terminus) for detection. Clones of

anti-Ras antibodies used were: RAS10 (pan-Ras-specific, Millipore); D2H12 (G12V-specific), or D8H7 (G12D-specific) (Cell Signaling Technology). Fluorophore-labeled secondary antibodies were purchased from Thermo Scientific. Anti-GFP (clone RQ2, MBL) was used for GFP pulldown experiments. BSA was from New England BioLabs. ELISA was performed with GFP ELISA Kit (Cell Biolabs) or p53 SimpleStep ELISA Kit (Abcam) according to the manufacturer's instructions.

Antibody conjugation. Antibodies were labeled with biotin or organic fluorophores via NHS-reactive ester. For biotin conjugation, antibodies were incubated with 50-fold molar excess of NHS-LC-biotin (Thermo Scientific) for 30-60 min and then isolated on 7 kD gel filtration columns (Thermo Scientific). For dye conjugation, antibodies were pre-captured on protein G magnetic beads and incubated with 10-fold molar excess of Alexa Fluor-NHS dye (Thermo Scientific) for 30-60 min. Free dye was washed out, and antibodies were further purified on 7 kD gel filtration columns (Thermo Scientific). Degree of labeling and concentration was measured by spectrophotometry.

Cells. TC-1 tumor cells were previously generated in our laboratory and have been reported[29]. Cells carrying mutant p53 (CFPAC-1 (C242R), OVCAR3 (R248Q), and TOV-112D (R175H)), cells with wildtype p53 (MCF-7, MCF-10), HEK 293 cells, and BHK21 cells were obtained from ATCC. Cells were cultured in RPMI-1640 medium or DMEM with 10% FBS and maintained under 5% CO_2 atmosphere. Lysate was prepared with commercial buffer containing 10% Triton X-100 in Tris-HCl (Abcam). Harvested supernatant was centrifuged at 10,000×g for 10 min and then passed through 0.22 μm filters to remove debris.

Mice. 6- to 8-week old female C57BL/6 and athymic nude (*Foxn1⁻/⁻*) mice were obtained from the National Cancer Institute. All animal procedures complied with protocols approved by the Johns Hopkins Institutional Animal Care and Use Committee and with recommendations for the proper use and care of laboratory mice.

Capture surface passivation. A borosilicate glass substrate of 130-170 μm thickness and 22×22 mm area was chosen for the capture surface. The substrate was first cleaned with ultrapure Milli-Q water (Millipore) in an ultrasonic bath for 10 min, dried under a stream of filtered air, exposed to high power atmospheric plasma (Plasma Etch, PE25-JW) for 5 min for surface activation, and then immediately dipped in methanol containing 1% *N*-(2-aminoethyl)-3-aminopropyltrimethoxysilane and 5% glacial acetic acid. The substrate was washed thoroughly with methanol and ultrapure water, dried under a stream of filtered air, and conjugated with biotin-mPEG-SVA (0.3 mg) in 10 mM sodium bicarbonate (pH 8.5) for 12 hr. The glass surface was then conjugated with a mixture of biotin-mPEG-SVA (0.3 mg) and PEG-mSVA (16 mg) (1:50 mass ratio) for 12 hr. After passivation, the substrate was washed with ultrapure water and dried as described above. The substrate was transferred to a clean container, vacuumed, flushed with pure nitrogen, sealed, and stored at -20°C.

Fabrication of SiMSI chip enclosure. The SiMSI chip was synthesized by photolithography. Briefly, a silicon wafer was rinsed with acetone and isopropanol, and then dehydrated at 200°C. The wafer was exposed to high power oxygen plasma (100 W for 3 min at 300-500 mTorr oxygen pressure) to promote photoresist adhesion. SU-8 photoresist was spin-coated onto the wafer to 100 μm thickness. The wafer was then soft-baked (65°C/95°C) and exposed to UV light in a mask aligner loaded with a mask printed

at 32,512 DPI resolution. The wafer was then hard-baked (65°C/95°C). The first layer of the SiMSI chip consists of the main channel with side boxes while the second layer consists of the arrays of staggered herringbone grooves. After all layers of photoresist were deposited, the wafer was developed under ultrasonic agitation to yield a master template for synthesis of the silicone elastomer chip enclosure. To produce this enclosure, PDMS elastomer was mixed with curing agent in a 10:1 ratio (by weight), poured onto the patterned wafer, degassed, and incubated at 80°C overnight. The PDMS was then removed from the master, cut into individual devices, and bored with inlet/outlet tubing holes (750 μm diameter). The devices were washed in an ultrasonic bath with isopropanol for 20 min and then with ultrapure water for 5 min. Devices were dried under a stream of filtered air.

Assembly of SiMSI chip. Prior to bonding, the coated glass substrate was attached to an alignment guide patterned with an imprint matching the shape and size of the flow channel. An elastomer cover fabricated with μm precision to the exact dimensions of the flow channel was then placed on top of the glass surface at the position of the channel imprint on the alignment guide. This cover permits the glass surface to be activated for bonding via oxygen plasma while preserving the high-density PEG/biotin-PEG passivation in the flow channel. Absence of this cover would cause the PEG/biotin-PEG layer to be destroyed by oxygen plasma bombardment. The coated glass surface (with elastomer cover) and PDMS devices were placed inside a plasma etcher and treated with oxygen plasma for 30 sec at 40 W RF power under 300-400 mTorr oxygen atmosphere. The elastomer cover was removed, and PDMS devices were then sealed to the coated glass substrate under a stereomicroscope with the alignment guide as a reference for the channel position. Chips were incubated at 80°C for 3 min to drive the bonding to completion.

Capture reagent conjugation to the SiMSI chip. Reagent introduction, removal, and wash steps were performed under automated flow actuated by a multi-channel peristaltic pump. SiMSI chips were connected to connected to inlet and outlet polytetrafluoroethylene tubing, and equilibrated with 10 mM Tris-HCl pH 8.0, 50 mM NaCl, 0.05% Tween-20 (T50) buffer. Chips were incubated with NeutrAvidin (20 μl; 0.1 mg/ml) in T50 buffer for 10 min at 50 μl/min flow rate. Chips were then washed with T50 buffer (1 ml) at 500 μl/min and incubated for 30 min with capture antibodies (2 μl; 0.1-1 mg/ml) in T50 buffer with 0.1 mg/ml BSA (T50-BSA). Chips were then washed with T50-BSA (1 ml) at 500 μl/min.

Sample circulation. Continuous circulation was actuated by a multi-channel infusion/withdrawal pump (bidirectional flow) connected to SiMSI chips via 26-gauge 1-cc syringes. Chips were connected at the other tubing port to the sample prepared in T50-BSA buffer. The presence of Tween-20 in the sample buffer is critical for preventing absorption of target proteins to the hydrophobic PDMS walls. For circulation, the pump was programmed to carry out repeated infusion/withdrawal cycles at 500 μl/min for 2-4 hr. After circulation, chips were washed with T50-BSA buffer (1 ml) at 500 μl/min, incubated with fluorophore-labeled detection antibodies for 30 min, and then washed again.

Single-molecule TIRF microscopy. An objective-based TIRF setup was employed with a 60× objective of high numerical aperature (>1.45). The incident laser angle was adjusted to full TIRF mode with a prism. Flow channels in the SiMSI chip were identified by patterned side boxes, which delineate the boundaries of the channel. An imaging region of 150×150 pixels, which translates to a physical area of 625 μm^2, was then set. The size of this region corresponds to the approximate size of the laser spot. An

EMCCD camera (Andor) was programmed to capture a time stream of 500 consecutive frames with 50 ms exposure time under continuous laser excitation of 10-20 mW. After imaging each region, the stage was displaced 50 μm down the length of the channel, and imaging was performed again as above. This process was repeated until at least 10 micrographs were recorded per sample.

Digital molecule quantification. Single-molecule TIRF data was analyzed with the ThunderSTORM program. In the quantification algorithm, a test was first applied to every pixel p in an imaging area of 150×150 pixels. The criteria for this test were that: (1) p has an intensity value that exceeds a defined threshold value, and (2) the intensity value of p exceeds the intensity value of all its four xy neighboring pixels. If p satisfies the criteria above, then it was chosen for further data processing; otherwise, p was excluded.

The exact positions of fluorophore-labeled target molecules within each pixel p that passed the above test were then determined by analysis of its point spread function. The number of target molecules with unique positions was counted; molecules separated in the imaging field by a distance below a certain value (for example 1-50 nm) were considered a single entity and hence only counted once. Molecules that occupied identical positions over multiple imaging frames were merged to compensate for blinking or slow photobleaching. Thus, the final readout was the total number of unique fluorophore-labeled target molecules in each imaging field (displayed as 'counts per field').

The cutoff threshold was set individually for each target protein. To determine the threshold for a particular target molecule, a SiMSI calibration test similar to that described in **Supplementary Figure III-2a, b** was performed with two groups: (1) a defined concentration of the target protein in buffer (positive control), and (2) buffer only without

the target protein (negative control). The algorithm described above was applied to both groups, and the number of counts per field in each control was calculated over threshold intensities ranging from 10^3 to 1.6×10^4. The number of counts per field in the positive control was divided by that in the negative control at each threshold value to compute the signal-to-noise ratio for that threshold value. The threshold that yielded the highest signal-to-noise ratio was chosen for SiMSI analysis of the particular target protein.

Single-molecule structural analysis. The first frame of 500 in each imaging region was isolated and stacked into a micrograph series. A wavelet filter was applied, and fluorescent spots that scored >1.3 standard deviations above the mean intensity in an eight-molecule neighborhood were selected for analysis. Individual molecule spatial coordinates were determined by integrated Gaussian multiple-emitter fitting. The σ values of each molecule were interrogated, and spots with σ within the 25-75 percentile were selected for further processing. Fluorescence intensity values were examined to characterize the size distribution of protein complexes, and these values were converted to subunits per aggregate based on single probe intensity profiles. We created a program in MATLAB to automatically compute the average aggregate frequency based on pre-defined size criteria.

Transplanted tumor challenge. C57BL/6 or athymic mice (*n=5* per group) were inoculated with TC-1 tumor cells (10^5 per animal) by subcutaneous injection in the flank or oropharyngeal injection into the buccal mucosa. At different time points after tumor challenge, whole blood was collected from the tail vein and processed into serum for SiMSI. Tumor growth was monitored over time by visual inspection, palpation, and digital caliper measurement.

Spontaneous tumor induction. Athymic mice ($n=5$ per group) were administered plasmid DNA (10 μg each, 30 μl total volume) encoding Ras^{G12V}, SB13 transposase, luciferase, and either anti-p53 shRNA or mutant human p53^{R175H} by injection into the buccal mucosa. Immediately afterwards, mice received electroporation (eight pulses of 72 V, 50 ms duration, and 200 ms interval) at the injection site with an ECM830 device (BTX). Tumor burden was monitored over time by whole body luminescence imaging with an IVIS Spectrum device (PerkinElmer). At different time points after tumor challenge, whole blood was collected from the tail vein and processed into serum for SiMSI.

Digital autoantibody detection. Recombinant human p53 protein was biotinylated at the C-terminus in a site-specific manner using the BirA biotin protein ligase[30]. The purified biotinylated protein was conjugated to SiMSI chips. Plasma samples were diluted from 10^3-$10^6\times$ and circulated on SiMSI chips for 2 hr. Chips were then washed and incubated with Alexa Fluor 488-labeled goat anti-human IgG (Thermo Scientific) for 30 min. Chips were washed again and visualized by SiMSI.

p53 native PAGE and immunoblot. BHK21 cells were transfected using Lipofectamine 2000 with mutant or wildtype p53 constructs (0.1-20 μg DNA) in 6-well plates. After 16 hr, lysate was prepared with 18 mM CHAPS in TBS containing DNase and protease inhibitor. Lysate was added with 20% glycerol and 5 mM Coomassie G-250 dye then loaded onto a 3-12% native PAGE Bis-Tris gel (Invitrogen). Electrophoresis was performed in 50 mM Bis-Tris and 50 mM Tricine plus 0.02% Coomassie G-250 dye in the cathode buffer for 2 hr at 100 V. Proteins were transferred to a polyvinylidene membrane and stained with Coomassie G-250 dye. The membrane was fixed with 8% acetic acid for

20 min and destained with 100% methanol. p53 proteins were detected by immunoblot with DO-1 antibodies.
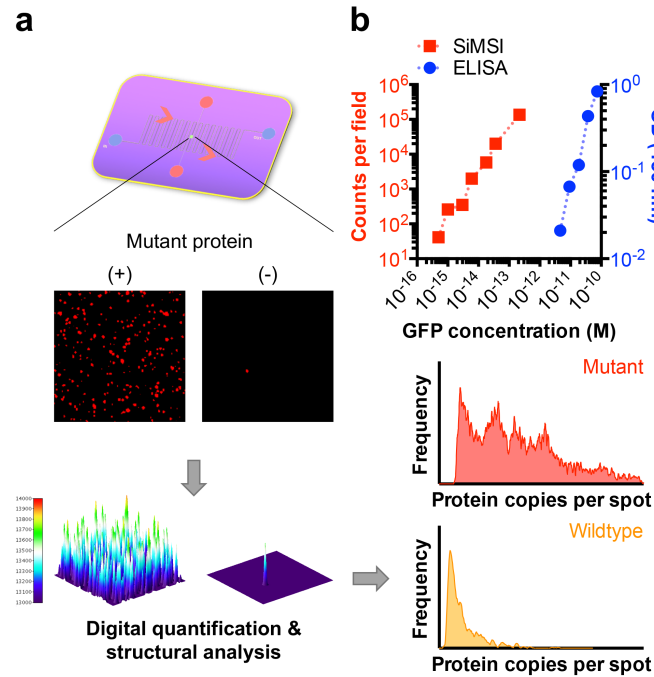
Figures

Figure III-1. Single-molecule structural imaging (SiMSI).

(**a**) Schematic diagram of the SiMSI platform. Circulating mutant tumor proteins are captured on a microfluidic chip and visualized by single-molecule total internal reflection fluorescence microscopy. Proteins that score above a set fluorescence threshold are digitally counted. By analysis of the spectrum of fluorescence intensities, the structural composition of target proteins is determined. (**b**) Comparison of the detection sensitivity of SiMSI and ELISA. For SiMSI, chips conjugated with anti-GFP antibodies were incubated with recombinant GFP at various doses. GFP was quantified by single-molecule imaging and presented as average counts per field (n=10).
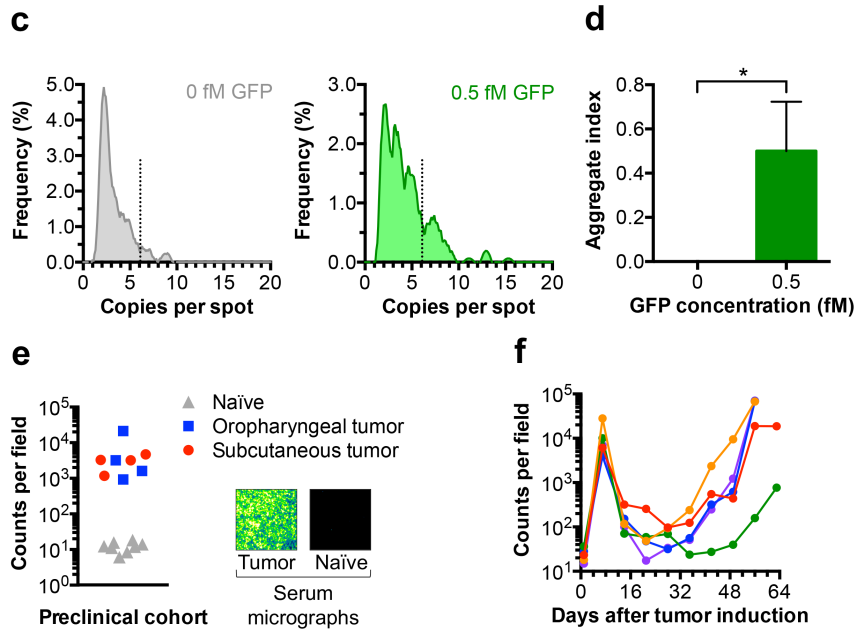
Figure III-1 (continued). Single-molecule structural imaging (SiMSI). (**c**) Structural protein analysis in the sub-fM concentration range. Histograms display the structural composition profile of 0.5 fM GFP or background (no GFP). (**d**) The frequency of GFP complexes at 0 or 0.5 fM was quantified. (**e-h**) SiMSI of cytoplasmic tumor proteins shed into the blood. (**e**) C57BL/6 mice were inoculated with TC-1 tumor cells carrying cytoplasmic GFP (CytoGFP) by oropharyngeal or subcutaneous injection. After two weeks, serum GFP was measured by SiMSI, and counts for individual mice are shown. (**f**) Tumor formation in athymic mice was induced via delivery of Ras^{G12V} and *shP53-GFP*. Plots of serum GFP counts over time in individual mice (*n=5*), assessed by SiMSI.
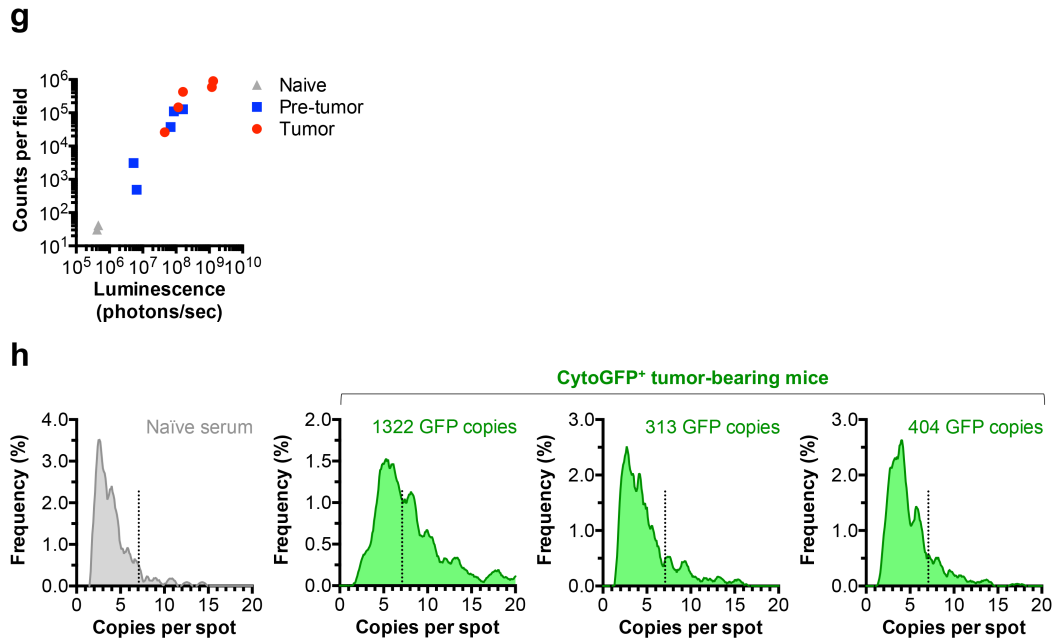
g

h

Figure III-1 (continued). Single-molecule structural imaging (SiMSI). (**g**) Tumor formation in athymic mice was induced via delivery of *Ras^{G12V}* and *shP53-GFP*. Relationship between circulating GFP levels and buccal luminescence in individual naïve, pre-tumor, and tumor-bearing mice (*n*=5 per group). (**h**) Structural analysis of circulating GFP in tumor-bearing mice. Histograms display GFP composition profile in naïve serum or serum from three representative mice with CytoGFP⁺ tumor.
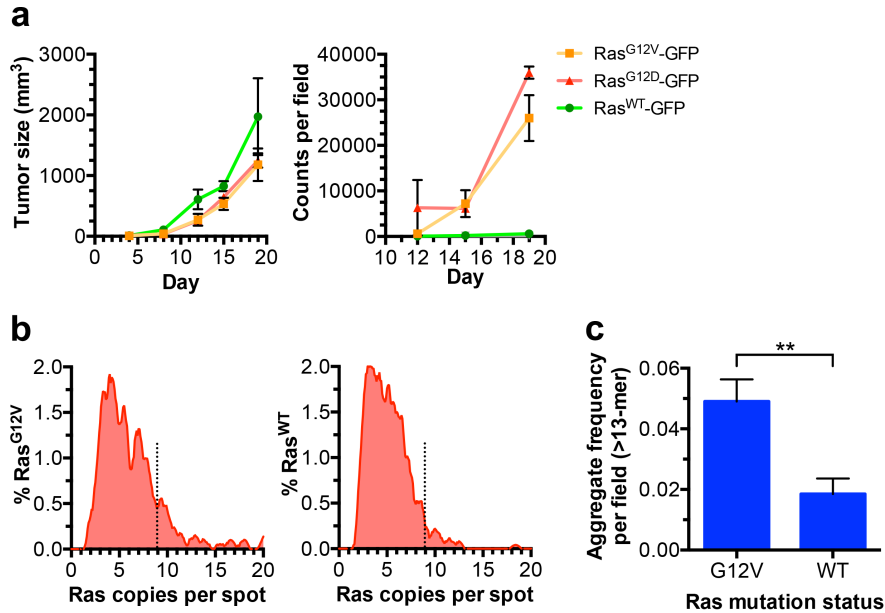
Figure III-2. Single-molecule imaging of circulating mutant tumor proteins.

(**a-c**) Analysis of mutant Ras. (**a**) Athymic mice were inoculated subcutaneously with tumor cells (TC-1) transduced with mutant (*Ras^G12V^-GFP, Ras^G12D^-GFP*) or wildtype (*Ras^WT^-GFP*) *Ras* oncogene. Tumor growth kinetics (left) or circulating Ras proteins (right) were characterized over time by single-molecule structural imaging (SiMSI). (**b, c**) Single-molecule analysis of Ras nanoclusters in tumor cells. Lysate from Ras^{G12V+} or Ras^{WT+} tumor cells was examined by SiMSI. (**b**) Structural profile of mutant or wildtype Ras in tumor cells. (**c**) The frequency of Ras nanoclusters (>13-mer size) in tumor cells with Ras^{G12V} or Ras^{WT} was quantified (**$P<0.01$)
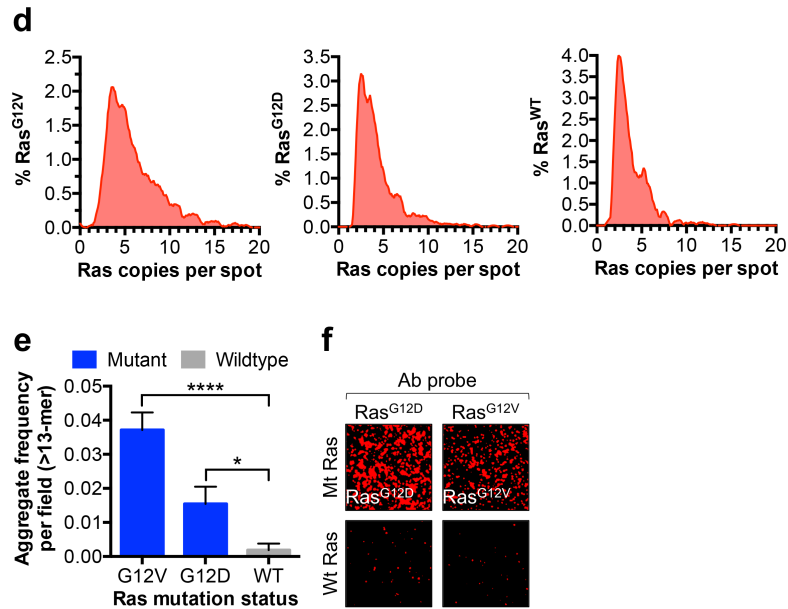
Figure III-2 (continued). Single-molecule imaging of circulating mutant tumor proteins.
(**d-f**) Analysis of mutant Ras. (**d, e**) Single-molecule analysis of circulating Ras nanoclusters. (**d**) Representative histograms display structural distribution of circulating mutant or wildtype Ras in tumor-bearing mice. (**e**) The frequency of circulating Ras nanoclusters was quantified (*$P<0.05$, ****$P<0.0001$). (**f**) Preferential detection of mutant Ras protein. HEK 293 cells were transfected with *Ras^{G12V}-GFP* or *Ras^{G12D}-GFP*. Ras proteins were captured and probed with antibodies that specifically recognize either the G12V or G12D mutant variant.
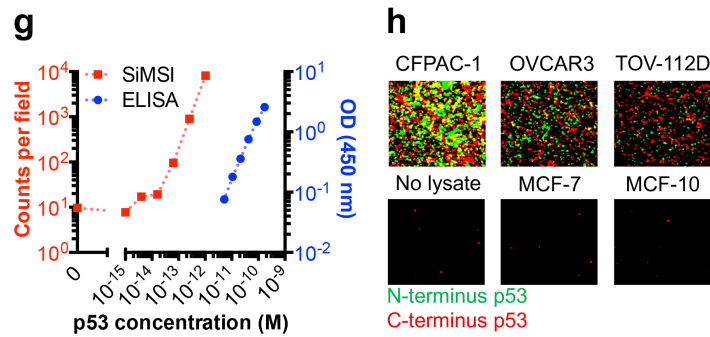
Figure III-2 (continued). Single-molecule imaging of circulating mutant tumor proteins. (**g, h**) Analysis of mutant p53. (**g**) Comparison of p53 detection sensitivity by SiMSI and ELISA. (**h**) Dual color SiMSI detection of mutant but not wildtype p53. Lysate from various tumor cells carrying mutant p53 (CFPAC-1 (C242R), OVCAR3 (R248Q), and TOV-112D (R175H)) or cells with wildtype p53 (MCF-7, MCF-10) was probed with antibodies against the N- or C-terminus of p53.
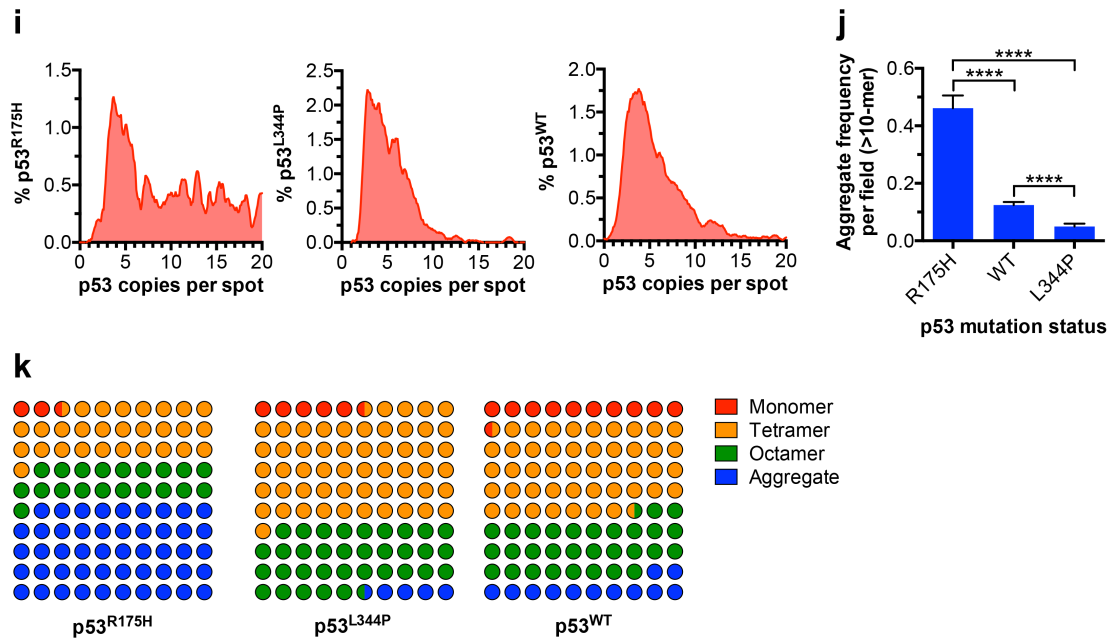
Figure III-2 (continued). Single-molecule imaging of circulating mutant tumor proteins. (**i-k**) Structural analysis of mutant p53. BHK21 cells transfected with mutant (p53[R175H], p53[L344P]) or wildtype (p53[WT]) p53 linked to GFP were interrogated by SiMSI. (**i**) Histograms display p53 structural profile, depicting the frequency of complexes containing indicated copies of p53. (**j**) The frequency of mutant or wildtype p53 complexes (>10-mer size) was quantified (****P<0.0001). (**k**) Color dot plots display the distribution of mutant or wildtype p53 into monomers, tetramers, octamers, or aggregates (>10-mer).
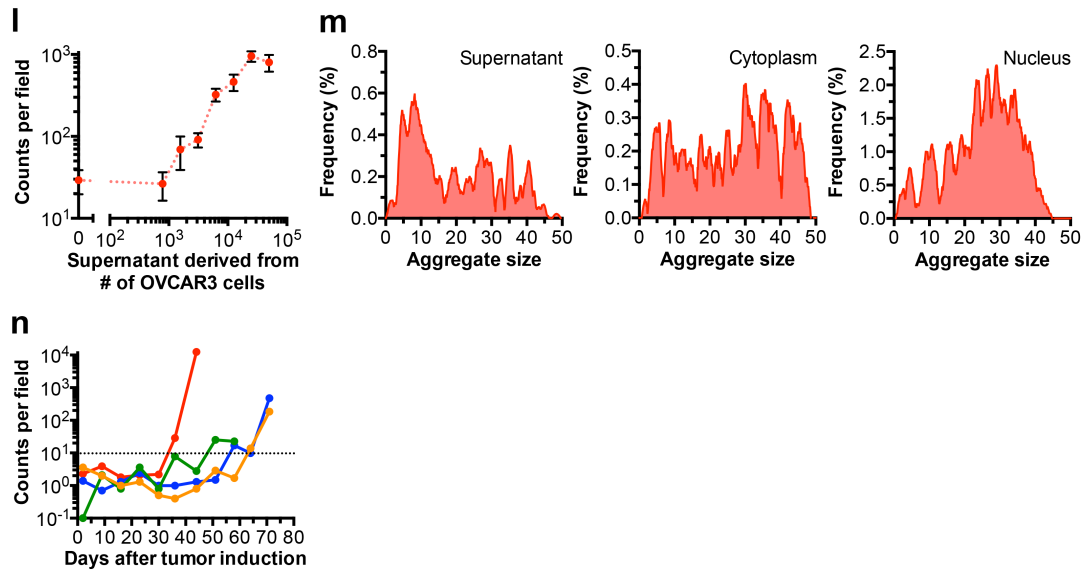
Figure III-2 (continued). Single-molecule imaging of circulating mutant tumor proteins.

(**l-n**) Analysis of mutant p53. (**l, m**) Single-molecule analysis of mutant p53 shed from human cancer cells. Ovarian cancer cells (OVCAR3) were seeded at various densities (10^3-10^5 cells/well). (**l**) Mutant p53 in filtered supernatant after 24 hr was measured by SiMSI. (**m**) OVCAR3 cells were fractionated into nucleus, cytoplasm, and supernatant. Histograms display the structural profile of mutant p53 in each compartment. (**n**) Kinetics of circulating mutant p53 release in a spontaneous tumor model. Tumor formation in athymic mice was induced via delivery of Ras^{G12V} and human $p53^{R175H}$. Plots of serum mutant p53 counts over time in individual mice, assessed by SiMSI.
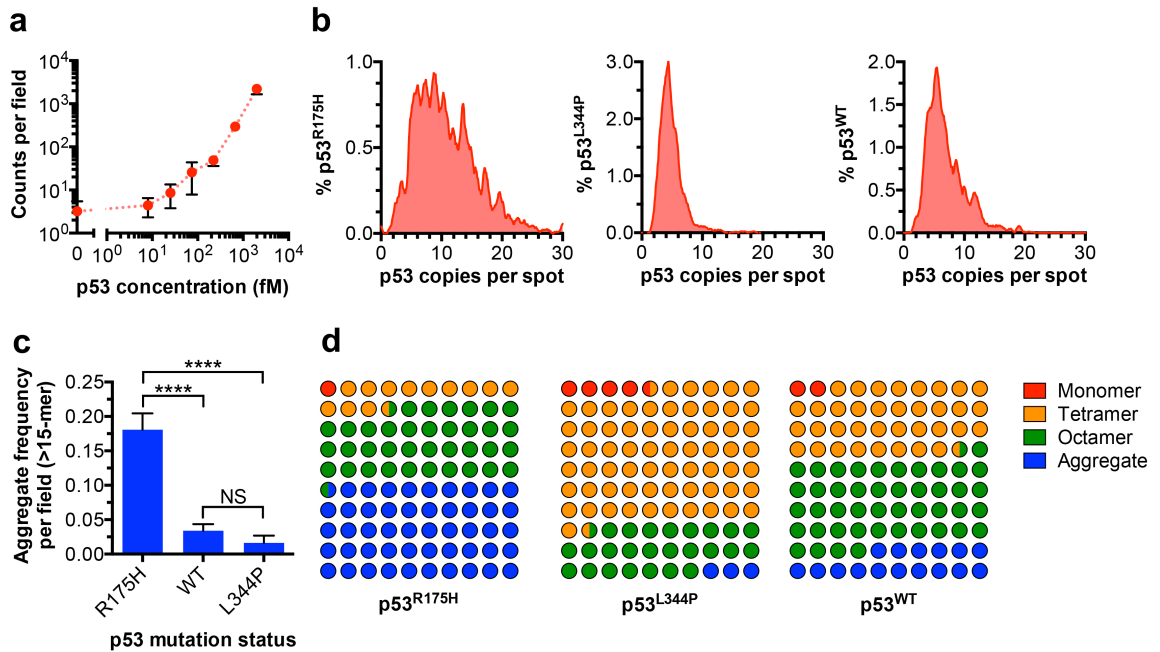
Figure III-3. Single-molecule analysis of circulating mutant p53 in cancer patients.
(**a**) Standard curve for p53 SiMSI in 50% normal human plasma. (**b-d**) p53 structural analysis in human plasma. BHK21 cells transfected with mutant (p53[R175H], p53[L344P]) or wildtype (p53[WT]) p53 linked to GFP were interrogated by SiMSI. (**b**) Histograms display p53 structural profile, depicting the frequency of complexes containing indicated copies of p53. (**c**) The frequency of mutant or wildtype p53 complexes (>15-mer size) was quantified (****P<0.0001; NS, not significant). (**d**) Color dot plots display the distribution of mutant or wildtype p53 into monomers, tetramers, octamers, or aggregates (>10-mer).
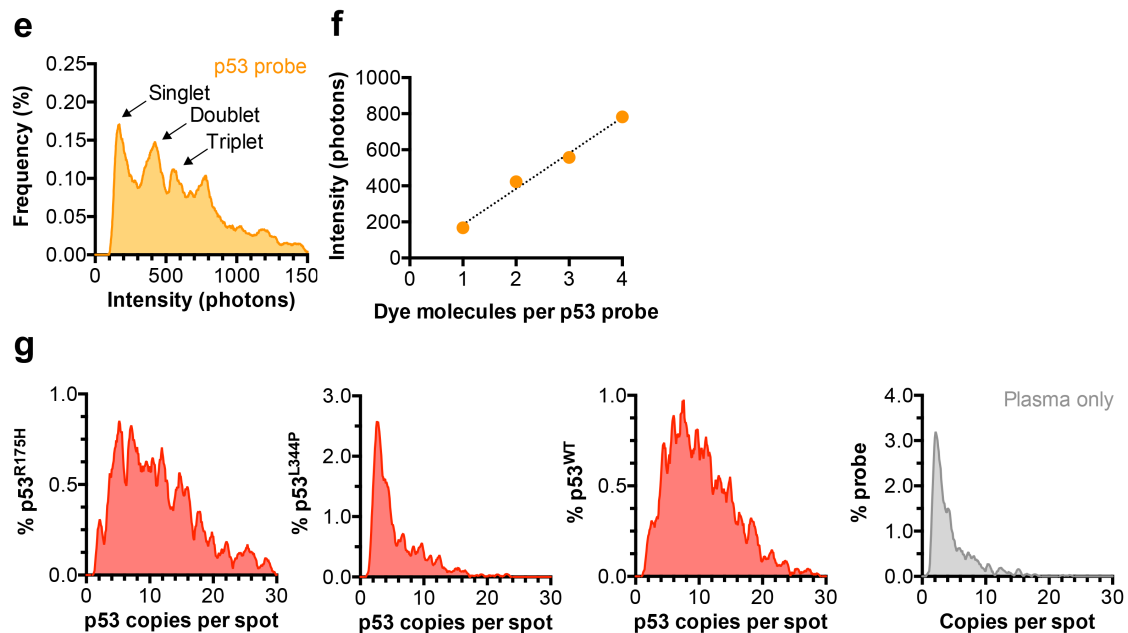
Figure III-3 (continued). Single-molecule analysis of circulating mutant p53 in cancer patients. (**e**) Fluorescence pattern of anti-p53 probe antibodies. Alexa Fluor 555-labeled p53 probe antibodies (100 fM) were precipitated on SiMSI chips with anti-isotype IgG. Molecule distribution into singlet, doublet, and triplet populations is shown. (**f**) Linear relationship between number of fluorophores per probe and intensity emitted. (**g**) Based on the p53 probe fluorescence pattern, the structural profile of p53[R175H], p53[L344P], and p53[WT] was characterized.
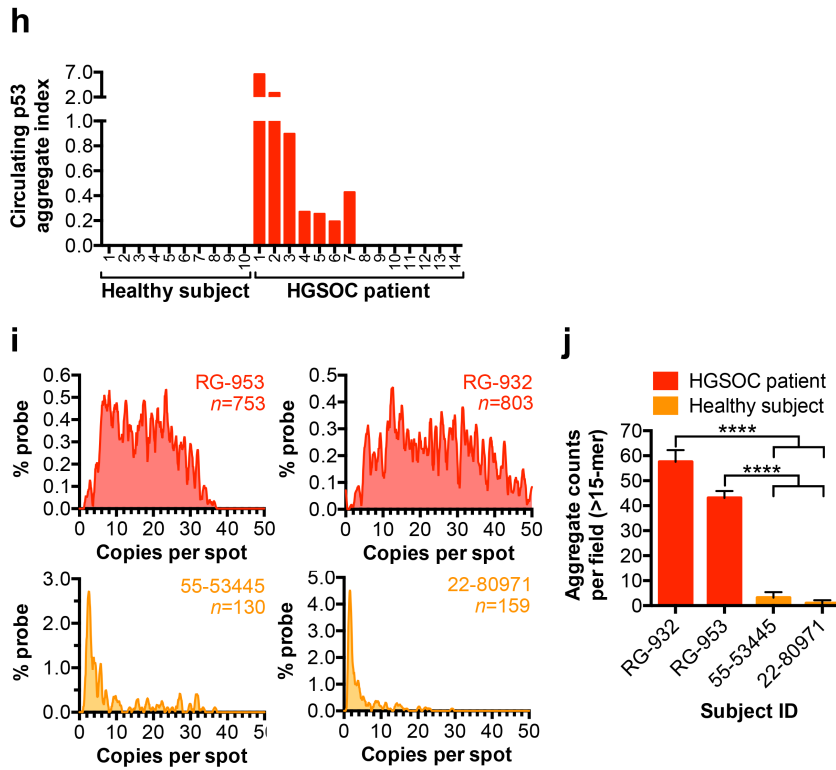
Figure III-3 (continued). Single-molecule analysis of circulating mutant p53 in cancer patients. (**h-j**) Single-molecule analysis of circulating mutant p53 in ovarian cancer. Plasma samples from healthy subjects (*n*=10) or high-grade serous ovarian cancer (HGSOC) patients (*n*=14) were interrogated for mutant p53 by SiMSI. (**h**) Number of circulating p53 complexes was quantified. (**i**) Structural profile of p53 distribution in two HGSOC patients (RG-953, RG-932) and two healthy subjects (55-53445, 22-80971). The *n* values represent the number of data points used for analysis. (**j**) The amount of p53 aggregates in HGSOC patients or healthy subjects (****P<0.0001).
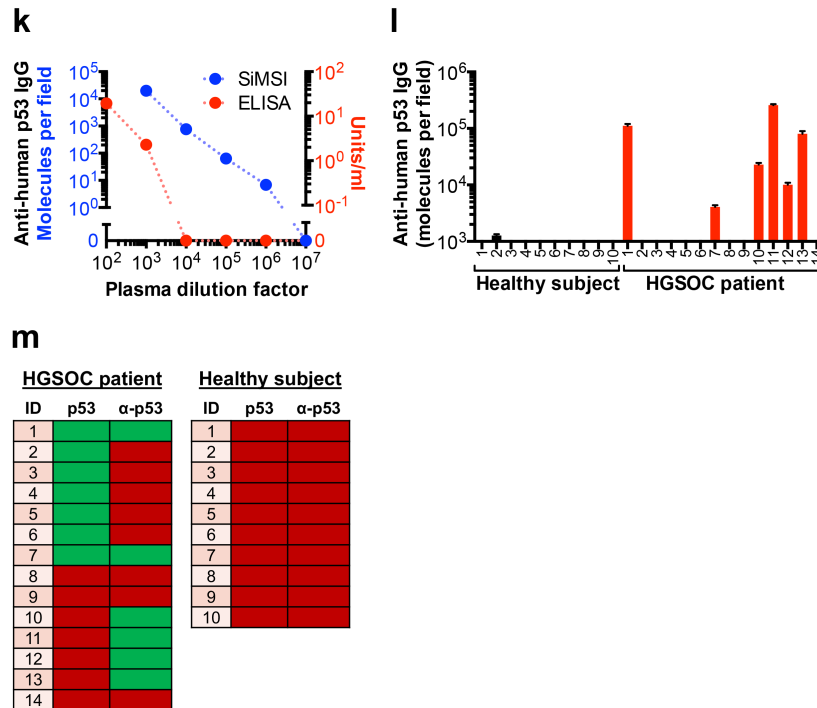
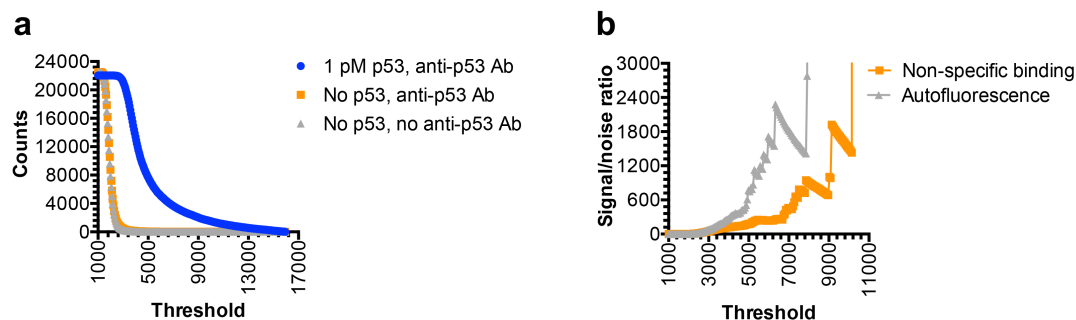*Figure III-3 (continued). Single-molecule analysis of circulating mutant p53 in cancer patients.* (**k**) Comparison of detection of anti-p53 autoantibodies by SiMSI or ELISA. (**l**) Circulating anti-p53 autoantibodies in individual subjects were measured by SiMSI. (**m**) Table summarizing complementary analysis of p53 and anti-p53 autoantibodies in HGSOC patients or healthy subjects by SiMSI (green: positive, red: negative).

Supplementary Figure III-1. Target molecule concentration via automated closed-loop circulation.

SiMSI chips conjugated with anti-GFP antibody were incubated with GFP for 30 min either with or without continuous circulation actuated via a bidirectional syringe pump. Chips were visualized by single-molecule imaging and GFP spots were measured. (**a**) Representative micrographs and (**b**) quantification (****$P<0.0001$).
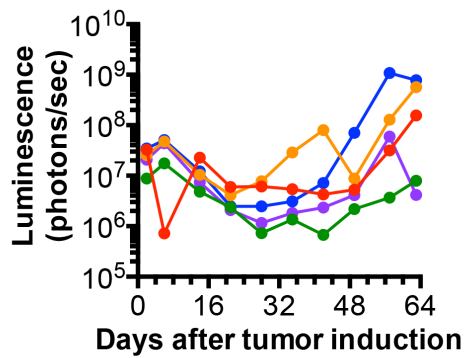
Supplementary Figure III-2. Dynamic threshold adjustment to maximize signal/noise ratio.

1 pM p53 or buffer only was added to SiMSI chips and probed with or without anti-p53 antibodies. (**a**) The number of fluorescence counts over 500 frames at different threshold intensities was digitally counted. (**b**) The signal/noise ratio for non-specific binding (1 pM p53 relative to no p53 in the presence of anti-p53 antibodies) or autofluorescence (1 pM p53 relative to no p53 in the absence of anti-p53 antibodies) was calculated at each threshold. At threshold values >9,000, the signal/noise ratio for 1 pM p53 detection exceeds 1,000. Furthermore, as the threshold increases, the signal/noise ratio rises exponentially.
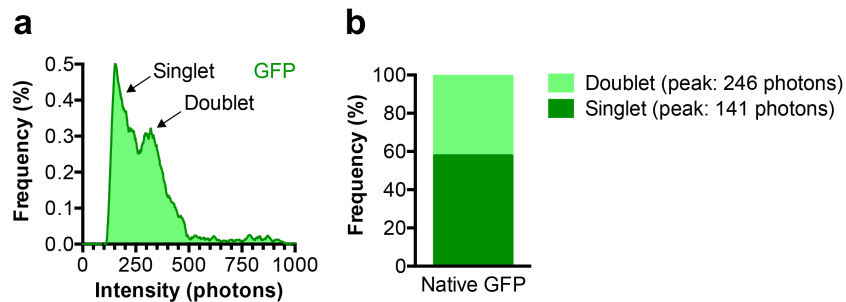
Supplementary Figure III-3. GFP fluorescence pattern.

Recombinant GFP (100 fM) was precipitated and examined by SiMSI. (**a**) Molecule distribution into singlet (peak emission: 141 photons) and doublet (peak emission: 246 photons) populations is shown. (**b**) Frequency of GFP singlet and doublet populations

Supplementary Figure III-4. Tumor progression kinetics in the spontaneous tumor model used to characterize the dynamics of cytoplasmic tumor protein release into blood.

Tumor formation in athymic mice was induced via injection of Ras^{G12V}, *shP53-GFP*, *Sb13* transposase, and *Luciferase* cDNA into the buccal mucosa followed by electroporation. Representative plots of buccal luminescence over time, an index of tumor growth, in individual mice (*n*=5).
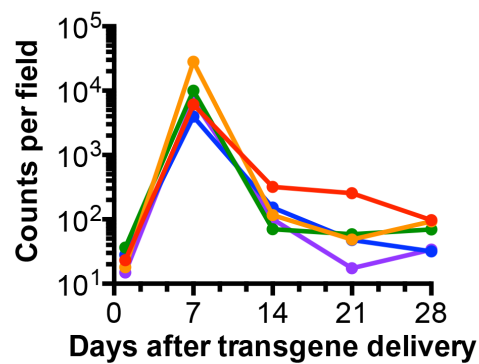
Supplementary Figure III-5. Kinetics of oncogene-induced release of nucleocytoplasmic proteins into the blood.

Athymic mice received transient delivery of Ras^{G12V} and *GFP* cDNA by injection into the buccal mucosa followed by electroporation. Plots depict the amount of serum GFP protein at different time points in individual mice (*n*=5) after transgene delivery.
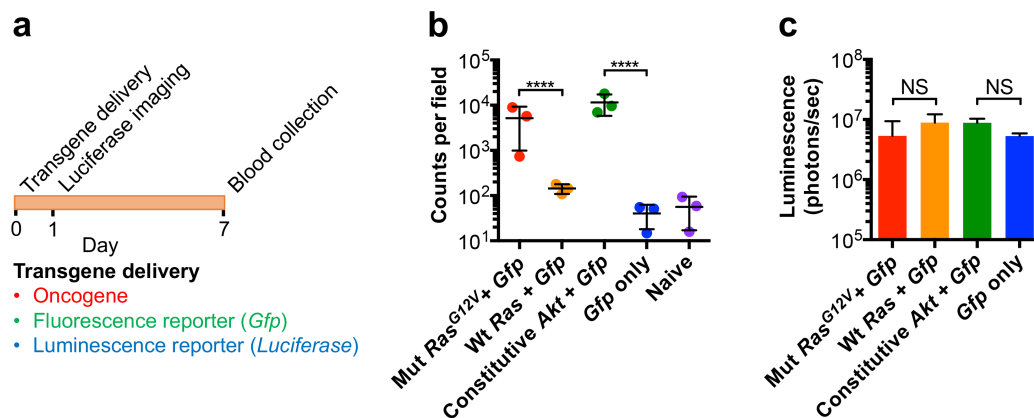
Supplementary Figure III-6. Oncogene-induced release of nucleocytoplasmic proteins from transformed cells into the blood.

(**a**) Schematic diagram of the experimental design. Normal cells were transformed *in vivo* by oncogene delivery into the buccal mucosa via electroporation. DNA encoding a cytoplasmic fluorescence reporter (GFP) as well as a luminescence reporter (luciferase) were concurrently administered. Local buccal luminescence imaging was performed one day after transgene delivery. Serum was collected at day seven, and GFP levels were assessed by SiMSI. (**b**) Circulating GFP counts in individual mice (*n*=3) that received various combinations of oncogene and GFP reporter (****P<0.0001). (**c**) Average buccal luminescence of mice in each group (NS, not significant).

87
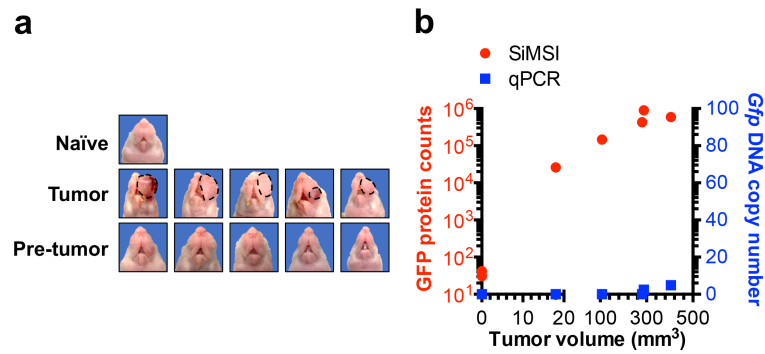
Supplementary Figure III-7. Serum levels of tumor-derived cytoplasmic proteins in a spontaneous tumor model as a function of tumor volume.

Tumor formation in athymic mice was induced via injection of Ras^{G12V}, *shP53-GFP*, *Sb13* transposase, and *Luciferase* cDNA into the buccal mucosa followed by electroporation. (**a**) Representative photographs of mice with visible tumor (after about seven weeks) or prior to the appearance of tumor ('pre-tumor'). (**b**) Serum GFP protein or DNA levels were measured in mice with established tumor by SiMSI or qPCR, respectively.
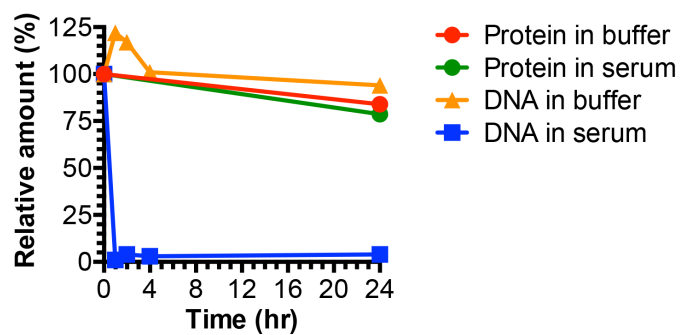
Supplementary Figure III-8. Comparison of the stability of GFP protein or DNA in the blood.

Purified GFP protein or DNA was spiked into mouse serum or Tris buffer control and incubated at 37°C for the indicated time periods. The amount of protein or DNA remaining at each time point was determined by SiMSI or qPCR, respectively. An identical molar amount of protein and DNA was added in each group.
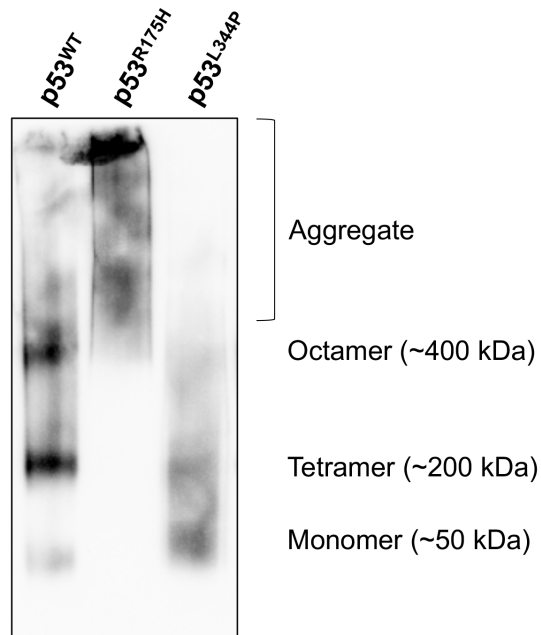
Supplementary Figure III-9. Native PAGE of mutant and wildtype p53. BHK21 cells were transfected with $p53^{WT}$, $p53^{R175H}$, *or* $p53^{L344P}$ *cDNA.*

Lysate was prepared, added with 20% glycerol and 5 mM Coomassie G-250 dye, and loaded onto a 3-12% native PAGE Bis-Tris gel for electrophoresis. After electrophoresis, proteins were transferred to a polyvinylidene membrane and probed with anti-p53 antibodies (clone: DO-1).
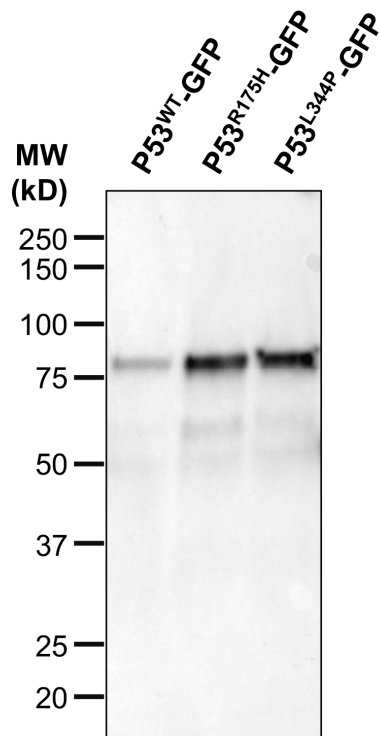
Supplementary Figure III-10. Immunoblot of mutant and wildtype p53-GFP.
BHK21 cells were transfected with *p53^{WT}-GFP, p53^{R175H}-GFP,* or *p53^{L344P}-GFP*. Lysate

was prepared for SDS-PAGE and immunoblot with anti-p53 antibodies (clone: DO-1).
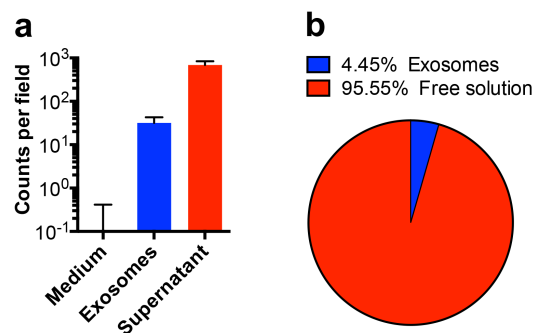
Supplementary Figure III-11. Distribution of mutant p53 protein shed from tumor cells.
(**a, b**) Conditioned supernatant was collected from human ovarian cancer cells (OVCAR3) and passed through a 0.22 µm filter to eliminate debris. Exosomes were isolated by ultracentrifugation. The amount of mutant p53 in exosomes or in the corresponding supernatant (depleted of exosomes) was measured by single-molecule analysis. Unconditioned medium served as a negative control. (**a**) Mutant p53 levels in exosomes or supernatant. (**b**) Pie chart depicting the percentage of p53 in exosomes or free in solution.
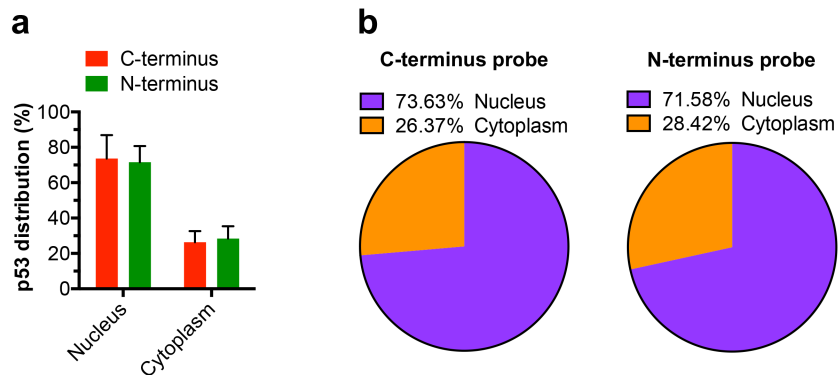
Supplementary Figure III-12. Analysis of mutant p53 organelle distribution in tumor cells by SiMSI.

Human ovarian cancer cells (OVCAR3; p53^{R248Q}) were fractionated into cytoplasm and nucleus, and both compartments were probed for p53 with dual N- and C-terminus fluorophore-labeled anti-p53 antibodies (clones Y5 and E47, respectively). The frequency of mutant p53 in the nucleus versus cytoplasm is depicted.
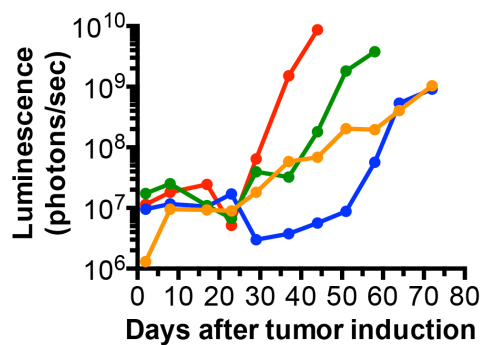
Supplementary Figure III-13. Kinetics of tumor growth in the spontaneous tumor model used to characterize the dynamics of mutant p53 protein release into blood.

Tumor formation in athymic mice was induced via injection of Ras^{G12V}, human $p53^{R175H}$, *Sb13* transposase, and *Luciferase* cDNA into the buccal mucosa followed by electroporation. Representative plots of buccal luminescence over time, an index of tumor growth, in individual mice (*n*=4).
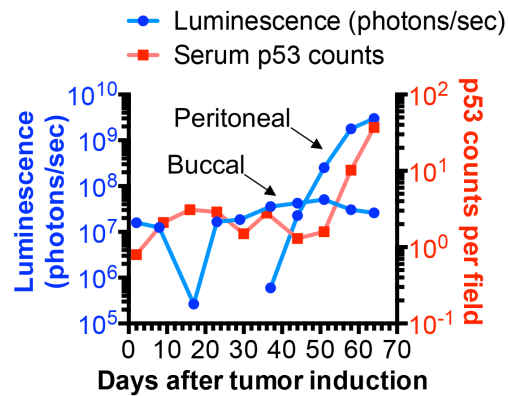
Supplementary Figure III-14. Monitoring distant tumor metastasis in real-time by SiMSI.
Tumor formation in athymic mice was induced via injection of Ras^{G12V}, human $p53^{R175H}$,
Sb13 transposase, and *Luciferase* cDNA into the buccal mucosa followed by
electroporation. In approximately 20% of mice, peritoneal metastasis is observed. Shown
is a representative plot from one of these mice, depicting both peritoneal and buccal
luminescence (blue), as well as serum p53 counts (red). Luminescence serves as an index
of local tumor load.
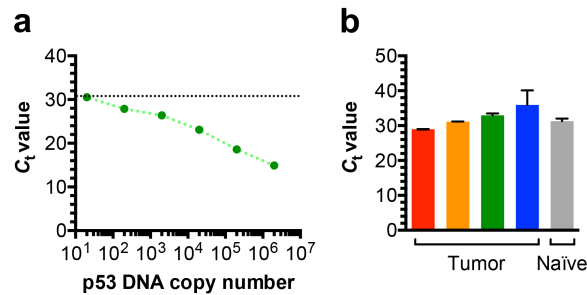
Supplementary Figure III-15. qPCR assay for detection of circulating mutant p53 DNA.
(**a**) Standard curve for qPCR detection of mutant p53 DNA. Different amounts of $p53^{R175H}$ plasmid DNA (from 20 to 2×10^6 copies) were subjected to qPCR, and C_t values were measured to generate a standard curve (R^2=0.9733). The dotted black line indicates the assay background in the presence of naïve mouse serum (C_t=31.3). The qPCR assay detection limit is 20 copies of p53 DNA. (**b**) Tumor formation in athymic mice was induced via buccal electroporation with Ras^{G12V}, human $p53^{R175H}$, *Sb13* transposase, and *Luciferase* (same cohort as in **Figure III-2n** with individual mice color-coded). Serum p53 DNA at the terminal time point was measured by qPCR. Naïve serum was included as a negative control.
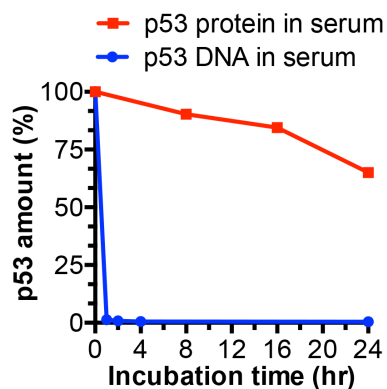
Supplementary Figure III-16. Comparison of the stability of p53 protein or DNA in serum.

p53 protein or DNA was spiked into mouse serum and incubated at 37°C for the indicated time periods. The amount of p53 protein or DNA remaining at each time point was determined by SiMSI or qPCR, respectively. An identical molar amount of protein and DNA was added in each group.
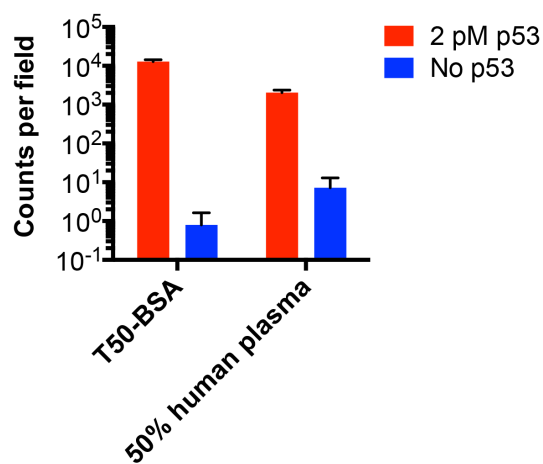
Supplementary Figure III-17. p53 detection by SiMSI in spiked normal human plasma.
50% normal human plasma was infused with p53 protein (2 pM) or left untreated and then subjected to SiMSI. The p53 signal and non-specific binding levels in human plasma relative to Tris buffer (T50-BSA) were measured.
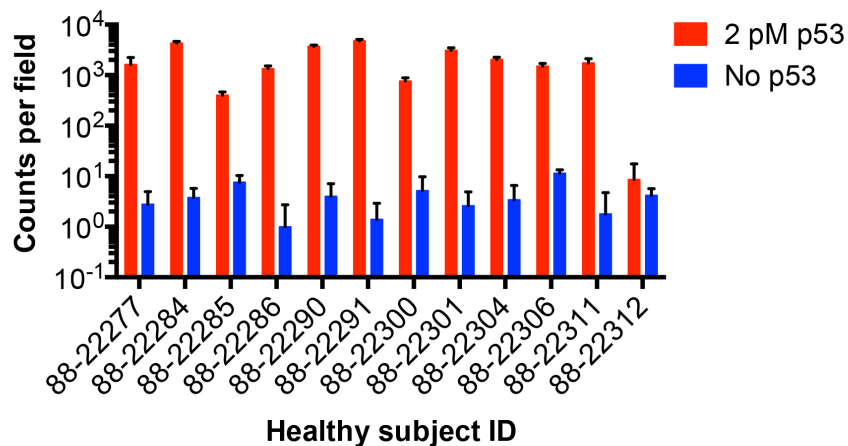
Supplementary Figure III-18. Background levels for p53 SiMSI in human plasma.
Individual plasma samples from a set of 12 randomly chosen human donors were spiked with or without p53 protein and subjected to SiMSI. Specific signal (2 pM p53) and non-specific background (no p53) levels are shown. For analysis of data from ovarian cancer patients (**Figure III-3g**), p53 counts >6 were considered positive. This cutoff corresponds to the upper limit of the 95% confidence interval of the data.
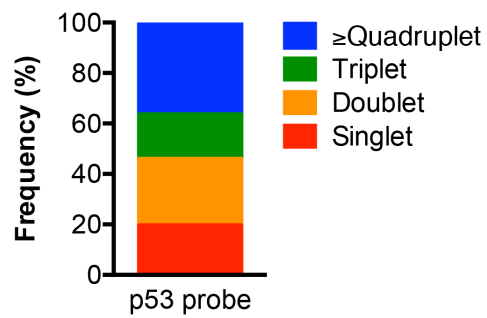
Supplementary Figure III-19. Fluorescence distribution of Alexa Fluor 555-labeled p53 probe antibodies.

Each color-coded region indicates the frequency of antibodies labeled with one (single),

two (doublet), three (triplet), or at least four (quadruplet) dye molecules.
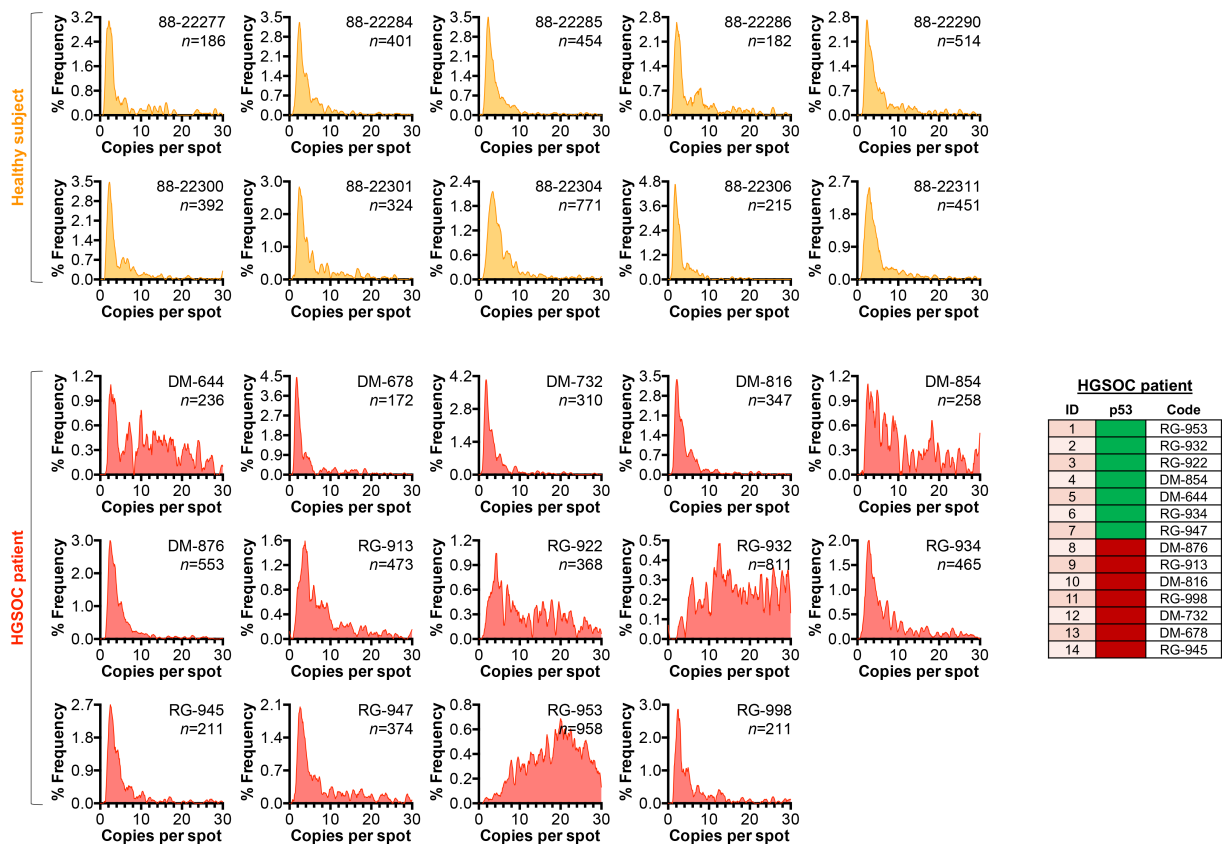
*Supplementary Figure III-20. Structural analysis of circulating p53 complexes in healthy subjects (*n=*10) and high-grade serous ovarian cancer (HGSOC) patients (*n=*14).*
Histograms display the frequency of complexes containing the indicated number of protein copies. *n* values denote the number of data points used for each sample analysis. The table lists the sample code corresponding to individual study subjects (**Figure III-3h, l, m**), as well as p53 status (green: positive, red: negative).
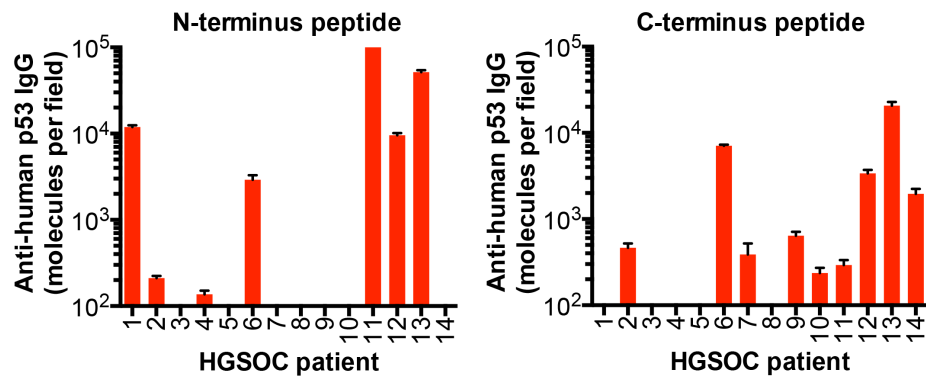
Supplementary Figure III-21. Assessment of autoantibodies against the N- or C-terminus of p53 by SiMSI.

Biotinylated p53 peptides derived from the N- or C-terminus were synthesized and conjugated to SiMSI chips. Plasma from high-grade serous ovarian cancer (HGSOC) patients was then passed through the chips and probed with Alexa Fluor 488-labeled anti-human IgG. The average number of copies of anti-human p53 IgG directed against the N- or C-terminus of p53 per imaging field is shown.

References

1.   Cancer Genome Atlas Research, N. Integrated genomic analyses of ovarian carcinoma. *Nature* **474**, 609-615 (2011).

2.   Hartwell, L., Mankoff, D., Paulovich, A., Ramsey, S. & Swisher, E. Cancer biomarkers: a systems approach. *Nat Biotechnol* **24**, 905-908 (2006).

3.   Rissin, D.M. et al. Single-molecule enzyme-linked immunosorbent assay detects serum proteins at subfemtomolar concentrations. *Nat Biotechnol* **28**, 595-599 (2010).

4.   Hill, H.D. & Mirkin, C.A. The bio-barcode assay for the detection of protein and nucleic acid targets using DTT-induced ligand exchange. *Nat Protoc* **1**, 324-336 (2006).

5.   Nam, J.M., Thaxton, C.S. & Mirkin, C.A. Nanoparticle-based bio-bar codes for the ultrasensitive detection of proteins. *Science* **301**, 1884-1886 (2003).

6.   Thaxton, C.S. et al. Nanoparticle-based bio-barcode assay redefines "undetectable" PSA and biochemical recurrence after radical prostatectomy. *Proc Natl Acad Sci U S A* **106**, 18437-18442 (2009).

7.   Fredriksson, S. et al. Multiplexed protein detection by proximity ligation for cancer biomarker validation. *Nat Methods* **4**, 327-329 (2007).

8.   Fredriksson, S. et al. Protein detection using proximity-dependent DNA ligation assays. *Nat Biotechnol* **20**, 473-477 (2002).

9.   Niemeyer, C.M., Adler, M. & Wacker, R. Detecting antigens by quantitative immuno-PCR. *Nat Protoc* **2**, 1918-1930 (2007).

10. Ruzicka, V., Marz, W., Russ, A. & Gross, W. Immuno-PCR with a commercially available avidin system. *Science* **260**, 698-699 (1993).

11. Sano, T., Smith, C.L. & Cantor, C.R. Immuno-PCR: very sensitive antigen detection by means of specific antibody-DNA conjugates. *Science* **258**, 120-122 (1992).

12. Giljohann, D.A. & Mirkin, C.A. Drivers of biodiagnostic development. *Nature* **462**, 461-464 (2009).

13. Xu, J. et al. Gain of function of mutant p53 by coaggregation with multiple tumor suppressors. *Nat Chem Biol* **7**, 285-295 (2011).

14. Yang-Hartwich, Y., Bingham, J., Garofalo, F., Alvero, A.B. & Mor, G. Detection of p53 protein aggregation in cancer cell lines and tumor samples. *Methods Mol Biol* **1219**, 75-86 (2015).

15. Soragni, A. et al. A Designed Inhibitor of p53 Aggregation Rescues p53 Tumor Suppression in Ovarian Carcinomas. *Cancer Cell* **29**, 90-103 (2016).

16. Jain, A. et al. Probing cellular protein complexes using single-molecule pull-down. *Nature* **473**, 484-488 (2011).

17. Lee, H.W. et al. Real-time single-molecule co-immunoprecipitation analyses reveal cancer-specific Ras signalling dynamics. *Nat Commun* **4**, 1505 (2013).

18. Jain, A., Liu, R., Xiang, Y.K. & Ha, T. Single-molecule pull-down for studying protein interactions. *Nat Protoc* **7**, 445-452 (2012).

19. Stroock, A.D. et al. Chaotic mixer for microchannels. *Science* **295**, 647-651 (2002).

20. Snapp, E.L. et al. Formation of stacked ER cisternae by low affinity protein interactions. *J Cell Biol* **163**, 257-269 (2003).

21. Zacharias, D.A., Violin, J.D., Newton, A.C. & Tsien, R.Y. Partitioning of lipid-modified monomeric GFPs into membrane microdomains of live cells. *Science* **296**, 913-916 (2002).

22. Polanski, M. & Anderson, N.L. A list of candidate cancer biomarkers for targeted proteomics. *Biomark Insights* **1**, 1-48 (2007).

23. Carlson, C.M., Frandsen, J.L., Kirchhof, N., McIvor, R.S. & Largaespada, D.A. Somatic integration of an oncogene-harboring Sleeping Beauty transposon models liver tumor development in the mouse. *P Natl Acad Sci USA* **102**, 17059-17064 (2005).

24. Prior, I.A., Lewis, P.D. & Mattos, C. A comprehensive survey of Ras mutations in cancer. *Cancer Res* **72**, 2457-2467 (2012).

25. Muller, P.A. & Vousden, K.H. p53 mutations in cancer. *Nature cell biology* **15**, 2-8 (2013).

26. Muller, P.A. & Vousden, K.H. Mutant p53 in cancer: new functions and therapeutic opportunities. *Cancer cell* **25**, 304-317 (2014).

27. Soussi, T. p53 Antibodies in the sera of patients with various types of cancer: a review. *Cancer Res* **60**, 1777-1788 (2000).

28. Goodell, V. et al. Antibody immunity to the p53 oncogenic protein is a prognostic indicator in ovarian cancer. *J Clin Oncol* **24**, 762-768 (2006).

29. Rodina, A. et al. The epichaperome is an integrated chaperome network that facilitates tumour survival. *Nature* **538**, 397-401 (2016).

30.   Lin, K.Y. et al. Treatment of established tumors with a novel vaccine that enhances major histocompatibility class II presentation of tumor antigen. *Cancer Res* **56**, 21-26 (1996).

31.   Chattopadhaya, S., Tan, L.P. & Yao, S.Q. Strategies for site-specific protein biotinylation using in vitro, in vivo and cell-free systems: toward functional protein arrays. *Nat Protoc* **1**, 2386-2398 (2006).

IV. Chapter 4. Conclusions and future directions

Applications of single-molecule structural imaging to cancer profiling. The single-molecule imaging technology we introduced is extremely versatile. Here we demonstrated its ability to identify and characterize circulating mutant tumor proteins and their associated complexes at a structural level. Notably, the applications of SiMSI are not limited to mutant tumor proteins or their autoantibodies. For example, we have found that, due to its single-molecule resolution and digital format, SiMSI quantifies conventional tumor-associated proteins, such as CA-125 or FOLR, with markedly greater sensitivity and accuracy than ELISA. Therefore, this technology holds the potential to transform existing clinical cancer biomarker assays.

We believe the next-generation applications of this technology, however, are even more exciting. It is now well-established that mutant oncoproteins and tumor suppressor proteins do not act in isolation, but often co-opt entire signaling machineries to mediate cancer progression. By direct inference, single-molecule imaging could be employed to dissect these signaling machineries within the tumor, for instance from tissue biopsies. Intriguingly, we speculate that these machineries may also be shed into the bloodstream, where they would be accessible to minimally invasive imaging technology, such as SiMSI. Thus, this technology provides the opportunity to decipher the intricate signaling networks of tumor cells from a blood sample. This information could identify the presence of cancer, help refine a diagnosis, and even point to effective treatment options.

In order to reach this stage, several key features must be incorporated into the SiMSI platform. First, our system is currently capable of tracing up to four unique

fluorophore-labeled antibodies at a time, which allows us to visualize four distinct proteins in a signaling complex. For instance, in the case of p53, we could design the system to reveal not only p53 clusters, but also p53 associated with its binding partners p63, p73, and heat-shock proteins. We envision that combinatorial color barcoding schemes could exponentially increase the number of unique proteins that could be detected in a single complex at one time.

In addition, we employed a multiplex, parallel channel design in the SiMSI microfluidic device, permitting two proteins to be examined in a single sample. As many different oncoproteins or tumor suppressor proteins could be altered in malignant cells, however, it is desirable to expand the number of mutant proteins that can be interrogated simultaneously. To achieve this, the chip could be engineered with a massive number of parallel channels segregated from each other via pneumatic valves. Alternatively, capture antibodies could be spot-printed rather than infused onto the chip surface. We are currently exploring these strategies with the goal of scaling the SiMSI chip up to a high-throughput format. We foresee that in the future, proteomic analysis could be conducted by SiMSI to characterize a broad panel of oncoproteins, tumor suppressor proteins, transcription factors, signaling mediators, and secondary messengers involved in cancer progression, and to map out their biochemical interactions.

Similar analysis could be performed to identify autoantibodies against tumor antigens. Though the idea of searching for autoantibodies in serum from cancer patients was first conceived long ago, techniques to probe for these autoantibodies have been hampered by low sensitivity and potential background contamination. By contrast, SiMSI possesses over 1,000 times the sensitivity of these conventional methods and could thus

shift the landscape of cancer autoantibodies. It will be intriguing to harness SiMSI in proteomic analysis to screen for cancer autoantibodies.

Applications of single-molecule structural imaging to identify tumor neoantigens. Perhaps one of the most exciting applications of SiMSI is in the discovery and validation of tumor neoantigens that can be targeted by immunotherapy. We have shown that this system is able to identify circulating mutant tumor proteins; these proteins comprise a pool within which to look for suitable neoantigens. We are currently building a SiMSI platform to functionally screen mutant tumor antigens. In our design, candidate mutant epitopes are loaded onto MHC class I proteins conjugated to the chip surface via a multimeric scaffold. PBMCs are lysed to solubilize T cell receptors (TCRs), which are then infused into the chip. We then probe for TCR occupancy on the mutant peptide-MHC (pMHC) proteins, which serves as an index of the number of systemic T lymphocyte precursors that recognize the candidate mutant epitopes. We believe that this system may evolve into a technology for selecting optimal tumor neoantigens for vaccination.

Programmed pMHC self-assembly as a powerful technology for vaccination against tumor neoantigens. The vaccination technology we introduced, in which pMHC polymerization is triggered on the plasma membrane via ANXA5 to drive activation of low-affinity cognate T cells, may represent a useful tool to generate immune responses against tumor neoantigens. Once the mutant epitopes associated with the greatest TCR abundance are elucidated by single-molecule imaging, recombinant DNA techniques can be applied to link these epitopes to β2 microglobulin, MHC class I heavy chain, and ANXA5 to derive a vaccination platform. While this is a robust process, the synthesis and validation of the chimeric protein can be time-consuming. To overcome this hurdle, we

propose that a generic 'empty' recombinant protein consisting of β2 microglobulin, MHC class I heavy chain, and ANXA5 but without peptide fusion can instead be created. This protein can then be loaded with mutant tumor epitopes and covalently conjugated at the peptide-binding groove. We envision that this type of universal design would allow for rapid development of vaccination against many distinct tumor neoantigens.

Closing remarks. The renaissance of cancer immunotherapy in the 21st century has ushered in unprecedented opportunities to control cancer growth in the long term and to eradicate metastasis. As we delve deeper into the web of interactions between tumor cells and the immune system, signaling pathways and biochemical alterations that can be targeted for therapy are being unearthed at breathtaking pace. The discovery that endogenous immune responses are naturally directed against mutant tumor antigens exemplifies the power of basic science understanding to translate into clinical breakthroughs. As the spectrum of possible tumor neoantigens continues to grow and methods to modulate the tumor microenvironment become increasingly potent, it is essential that we have tools for profiling these mutant tumor antigens and for expanding the endogenous lymphocyte populations that recognize them. The technologies we have introduced were crafted to achieve this purpose. As these technologies continue to mature, they offer the potential to one day significantly reduce morbidity and mortality due to cancer.

Curriculum Vitae

Chih-Ping Mao
501 St. Paul St., #1302
Baltimore, MD 21202
E-mail: mao@jhmi.edu

EDUCATION

Johns Hopkins School of Medicine, Baltimore, MD   2009 – present
Medical Scientist Training Program
M.D. and Ph.D. in Immunology

Johns Hopkins University, Baltimore, MD   2005 – 2009
B.S. with Honors in Molecular and Cellular Biology

AWARDS AND HONORS

Best Poster Award, Johns Hopkins Immunology Program Retreat   2016

Pathology Young Investigator Day Award   2016

Best Poster Award, Johns Hopkins Immunology Program Retreat   2015

Pathology Young Investigator Day Award   2015

Michael A. Shanoff Research Award   2015

Pathology Young Investigator Day Award   2014

Ruth L. Kirchstein National Research Service Award   2013 – 2014

Medical Scientist Training Program Grant   2009 – present

Provost's Undergraduate Research Award   2008

Barry M. Goldwater Scholarship   2007

Provost's Undergraduate Research Award   2007

Institute for NanoBioTechnology Fellowship   2007

Provost's Undergraduate Research Award   2006

Johns Hopkins University Dean's List	2005 – 2009
M.D. Anderson Cancer Center Scholarship	2005
National Merit Scholarship	2005
National Advanced Placement Scholar	2005
Fidelity National Information Services Scholarship	2005 – 2009
Robert A. Welch Foundation Scholar	2004

HONARARY SOCIETIES

Phi Beta Kappa	2009
Tri Beta Biology Honor Society	2007
Golden Key International Honor Society	2007
Alpha Epsilon Delta Pre-Health Honor Society	2007
National Society of Collegiate Scholars	2006

ORIGINAL ARTICLES

Kang, T.H.*, **Mao, C.P.***, Lee, E.J., Kim, Y.S., Kim, K., Ryu, J.H., Chang, H., Yeo, W.S., Choi, I., Yang, A., Kim, T.W., Park, Y.M., Wu, T.C., Hung, C.F. TLR9 acts as a bifunctional sensor of tumor self-DNA and modulates the anti-tumor immune response following chemotherapy. *Submitted* (2017).
* Co-first authors

Lee, Y.H., Bae, H.C., Kim, J.H., Oh, S.J., Lee, H.J., Song, K.H., Hong, S.O., Woo, S.R., Lee, K.M., Yee, C., Kim, B.W., Cho, H., Chung, E.J., Chung, J.Y., Hewitt, S., **Mao, C.P.**, Wu, T.C., Kim, T.W. Metabolic reprogramming via ATP5H loss triggers multi-modality cancer therapy resistance. *Submitted* (2017).

Song, K.H., Choi, C.H., Lee, H.J., Oh, S.J., Woo, S.R., Hong, S.O., Noh, K.H., Cho, H., Chung, E.J., Kim, J.H., Chung, J.Y., Hewitt, S.M., Baek, S., Lee, K.M., Yee, C., Son, M., **Mao, C.P.,** Wu, T.C., Kim, T.W. HDAC1 upregulation by NANOG promotes multidrug resistance and a stem-like phenotype in immune-edited tumor cells. *Cancer Research,* 77:5039-5053 (2017).

Lee, S.J., Song, L., Yang, M.C., **Mao, C.P.**, Yang, B., Yang, A., Jeang, J., Peng, S., Wu, T.C., Hung, C.F. Local administration of granulocyte macrophage colony-stimulating factor induces local accumulation of dendritic cells and antigen-specific CD8^{+} T cells and enhances dendritic cell cross-presentation. *Vaccine*, 33:1549-1555 (2015).

Lee, Y.H., Bae, H.C., Noh, K.H., Song, K.H., Ye, S.K., **Mao, C.P.**, Lee, K.M., Wu, T.C., Kim, T.W. Gain of HIF-1α under normoxia in cancer mediates immune adaptation through the AKT/ERK and VEGFA axes. *Clinical Cancer Research,* 21:1438-1446 (2015).

Kang, T.H., **Mao, C.P.**, Lee, S.Y., Chen, A., Lee, J.H., Kim, T.W., Alvarez, R.D., Roden, R.B., Pardoll, D.M., Hung, C.F., Wu, T.C. Chemotherapy acts as an adjuvant to convert the tumor microenvironment into a highly permissive state for vaccination-induced antitumor immunity. *Cancer Research*, 73:2493-2504 (2013).

Kang, T.H., **Mao, C.P.**, La, V., Chen, A., Hung, C.F., Wu, T.C. Innovative DNA vaccine to break tolerance against tumor self-antigen. *Human Gene Therapy*, 24:181-188 (2013).

Noh, K.H., Kim, B.W., Song, K.H., Cho, H., Lee, Y.H., Kim, J.H., Chung, J.Y., Kim, J.H., Hewitt, S.M., Seong, S.Y., **Mao, C.P.**, Wu, T.C., Kim, T.W. Nanog signaling in cancer promotes stem-like phenotype and immune evasion. *Journal of Clinical Investigation*, 122:4077-4093 (2012).

Kang, T.H., **Mao, C.P.**, He, L., Tsai, Y.C., Liu, K., La, V., Wu, T.C., Hung, C.F., Tumor-targeted delivery of IL-2 by NKG2D leads to accumulation of antigen-specific CD8^{+} T cells in the tumor loci and enhanced anti-tumor effects. *PLoS One*, 7:e35141 (2012).

Noh, K.H., Lee, Y.H., Jeon, J.H., Kang, T.H., **Mao, C.P.**, Wu, T.C., Kim, T.W., Cancer vaccination drives Nanog-dependent evolution of tumor cells toward an immune-resistant and stem-like phenotype. *Cancer Research*, 72:1717-1727 (2012).

Mao, C.P., Hung, C.F., He, L., Tsai, Y.C., Wu, T.C., *In vivo* microRNA-155 expression influences antigen-specific T cell-mediated immune responses generated by DNA vaccination. *Cell and Bioscience*, 1:3-13 (2011).

Mao, C.P., Hung, C.F., Kang, T.H., He, L., Tsai, Y.C., Wu, C.Y., Wu, T.C., Combined administration with DNA encoding vesicular stomatitis virus G protein enhances DNA vaccine potency. *Journal of Virology*, 84:2331-2339 (2010).

Chuang, C.M., Monie, A., Wu, A., **Mao, C.P.**, Hung, C.F., Treatment with LL-37 peptide enhances the antitumor effects induced by CpG oligodeoxynucleotides against ovarian cancer. *Human Gene Therapy*, 20:303-313 (2009).

Huang, B., **Mao, C.P.**, Peng, S., Hung, C.F., Wu, T.C., RNA interference-mediated *in vivo* silencing of FasL as a strategy for the enhancement of DNA vaccine potency. *Human Gene Therapy*, 19:763-773 (2008).

Huang, B., **Mao, C.P.**, Peng, S., Huang, C.H., He, L., Hung, C.F., Wu, T.C., Intradermal administration of DNA vaccines combining a strategy to bypass antigen processing with a strategy to prolong dendritic cell survival enhances DNA vaccine potency. *Vaccine*, 25:7824- 7831 (2007).

REVIEW ARTICLES AND BOOK CHAPTERS

Mao, C.P., Wu, T.C., Song, K.H., Kim, T.W. Immune-mediated tumor evolution: Nanog links the emergence of a stem-like cancer cell state and immune evasion. *OncoImmunology*, 3:e947871 (2014).

Mao, C.P., Wu, T.C., Applications of RNA interference technology to cancer research and treatment. *Methods in Molecular Biology*, 623:325-339 (2010).

Mao, C.P., Wu, T.C., Molecular pathogenesis of the human papillomavirus: cervical cancer as a model. *Translational Research in Biomedicine*, 1:20-36 (2007).

Mao, C.P., Lin, Y.Y., Hung, C.F., Wu, T.C., Immunological research using RNA interference technology. *Immunology*, 121:295-307 (2007).

Mao, C. P., Hung, C.F., Wu, T.C., Immunotherapeutic strategies employing RNA interference technology for the control of cancers. *Journal of Biomedical Science*, 14:15-29 (2007).

Mao, C.P., Hung, C.F., Wu, T.C., Cancer immunotherapy using RNAi. *European Pharmaceutical Review*, 12:13-19 (2007).

Mao, C.P., Hung, C.F., Wu, T.C. Cancer immunotherapy using RNA interference technology. *American Drug Discovery*, 1:1-6 (2006).

INVENTIONS AND PATENTS

Mao, C.P., Wang, S.C., Xiao, J., Hung, C.F., Wu, T.C. Non-invasive disease detection and diagnosis by single-molecule analysis (2016).

Mao, C.P., Wu, T.C., Hung, C.F., Programmed self-assembly of a peptide-MHC dynamic anchor for antigen-specific immune modulation (2014).

PRESENTATIONS

"Next-generation tools for cancer detection, diagnosis, and monitoring." Johns Hopkins School of Medicine Partnering Toward Discovery Symposium, Baltimore, MD, USA (2016).

"Programmed self-assembly of a peptide-MHC dynamic anchor for antigen-specific immune modulation." AAP/ASCI Annual Joint Meeting, Chicago, IL, USA (2015).

"Programmed self-assembly of a peptide-MHC dynamic anchor for antigen-specific immune modulation." AACR Annual Meeting, Philadelphia, PA, USA (2015).

"Programmed self-assembly of peptide-MHC for antigen-specific immune modulation." Johns Hopkins School of Medicine Young Investigator's Day, Baltimore, MD, USA (2015).

"Development of a new technology for activation of antigen-specific lymphocytes." Johns Hopkins School of Medicine Annual Immunology Retreat, Baltimore, MD, USA (2014).

"Release of self-DNA underlies the adjuvant effect of chemotherapy." Johns Hopkins School of Medicine Pathology Young Investigator's Day, Baltimore, MD, USA (2014).

"Combined administration of DNA encoding vesicular stomatitis virus G protein enhances DNA vaccine potency." 26th International Papillomavirus Conference and Workshops, Montreal, QC, CA (2010).

"A novel DNA vaccine that couples concentrated antigen transfer to dendritic cells with induction of the acute inflammatory response." Provost's Undergraduate Research Award Recognition Ceremony, Baltimore, MD, USA (2009).

"miR-155 expression in dendritic cells negatively regulates the activation of T cell-mediated immunity." Provost's Undergraduate Research Award Recognition Ceremony, Baltimore, MD, USA (2008).

"Polymeric drug delivery systems for the treatment of ovarian carcinoma." Institute for Nanobiotechnology Symposium, Baltimore, MD, USA (2007).

"Short hairpin RNA-mediated knockdown of Fas ligand in dendritic cells: A novel strategy for the potentiation of antitumor DNA vaccines." Provost's Undergraduate Research Award Recognition Ceremony, Baltimore, MD, USA (2007).

"Expression of *Foxn1* in the *p63* null thymus." M.D. Anderson Cancer Center Symposium, Smithville, TX, USA (2004).